atoms

MDPI

Article

Second-Order Rayleigh–Schrödinger Perturbation Theory for the GRASP2018 Package

Gediminas Gaigalas *, Pavel Rynkun and Laima Kitovienė

Institute of Theoretical Physics and Astronomy, Faculty of Physics, Vilnius University, Saulėtekio Ave. 3, LT-10257 Vilnius, Lithuania; pavel.rynkun@tfai.vu.lt (P.R.); laima.radziute@tfai.vu.lt (L.K.)
* Correspondence: gediminas.gaigalas@tfai.vu.lt

Abstract

A developed method, based on the stationary second-order Rayleigh–Schrödinger many-body perturbation theory in an irreducible tensorial form, allows us to determine the most important core–valence, core, core–core, and valence–valence correlations for any atom or ion with an arbitrary number of valence and core electrons. This paper presents the Feynman diagrams that describe these correlations. Additionally, it provides the rules for obtaining algebraic expressions in an irreducible tensorial form for any Feynman diagram coming from second-order many-body perturbation theory. Whereas some types of the valence–valence and core–valence correlations are described by the three-particle Feynman diagrams, additional developments to calculate the spin-angular parts of these diagrams have been made to the program library `libbrang` of the GRASP2018 As an example of the application of the developed method, the atomic calculations of the energy level structure and transition data for Ar II are presented.

Keywords: perturbation theory; valence–valence correlations; core–valence correlations; core correlations; core–core correlations.

1. Introduction

The General Relativistic Atomic Structure Package (GRASP) [1–6], which has been under development for decades, is one of the most effective tools available today for the theoretical study of the various properties of the atom. It allows the study of the energy spectrum, various transition characteristics, hyperfine structure, isotope shift with very high precision. The origin of this program lies with some of the most prominent and distinguished atomic theorists of recent times, Prof. Ian Philip Grant (1930–2025) and Prof. Charlotte Froese Fischer (1929–2024).

The GRASP software package is based on the multiconfiguration Dirac–Hartree–Fock (MCDHF) method and relativistic configuration interaction (RCI) method [7–9]. They have provided very accurate atomic data for a wide range of atoms and ions. These data have been used in various fields of science and technology. One of the most important conditions for obtaining such accurate atomic characteristics is the accurate incorporation of correlation and relativistic effects into the calculations. Correlation effects are included in these methods when the atomic state function (ASF) for which the eigenvalue problem is being solved is constructed from a set of configuration state functions (CSFs) containing the starting configuration and the other configurations constructed from it. The latter are obtained by performing single, double, or even sometimes triple and quadruple excitations on the initial configuration. This, if high accuracy is to be achieved, usually leads to a

Academic Editor: Kanti M. Aggarwal

Received: 7 April 2026
Revised: 14 May 2026
Accepted: 19 May 2026
Published: 21 May 2026

large CSF base. This base, therefore, needs to be limited. There are a number of methods/recommendations [7,8,10,11] for selecting the optimal CSF base to achieve the desired accuracy. But these recommendations are approximate, and, moreover, the choice of such a base is not trivial and requires much additional research, and, at the same time, it is not always possible to find the most optimal set of CSFs.

Recently, a new approach [12–17] has been proposed in which, based on the stationary second-order Rayleigh–Schrödinger many-body perturbation theory (RSMBPT) in irreducible tensorial form, it is theoretically possible, on an ab initio basis, to find a set of CSFs that are optimal in terms of the size of the CSF basis and that lead to maximally accurate atomic characteristics. It is based on a combination of RCI and RSMBPT in irreducible tensorial form. It allows the inclusion of core–valence (CV), core (C), core–core (CC), and valence–valence (VV) correlations using the second-order of perturbation theory for any atom and ion with any number of valence electrons. This newly developed method, which can be used in three ways (RCI + RSMBPT (see, for example, Section 4.1 in [12]), RCI (RSMBPT) (see, for example, Section 4.2 in [12]), and MCDHF (RSMBPT) (see, for example, Section 5.1.2 in [16]), allows for the reduction of the space of configuration state functions for complex atoms and ions, which extends the capability of the GRASP2018 software package [6].

In the RCI + RSMBPT method, the correlations considered in the RSMBPT method are added to the correlations considered in the conventional RCI method by adding them to the corresponding matrix elements from which the matrix is constructed in the RCI method (see, for example, for CV correlations, Equation (20) in [12]). In this method, the order of the matrix to be constructed is considerably reduced because correlations considered by the RSMBPT method are not represented by their own matrix elements in the matrix constructed by the RCI method.

In the RCI (RSMBPT) method, the value of the correlation influence on RCI calculations is assessed by considering all the correlation types separately according to ΔE_{PT} (see, for example, for CV correlations, Equation (22) in [12]) from the RSMBPT method. The most important correlations are then selected according to the criterion given, and these, together with the remaining correlations (which are not considered in the RSMBPT method), are included in the RCI calculation in a regular way (via the CSF expansion). In this case, the matrix constructed is of a higher order than the RCI + RSMBPT, but the correlations are included more consistently (not only in the second-order of perturbation theory). In both methods, only Coulomb interactions are considered for correlations investigated by the RSMBPT, which makes the RCI (RSMBPT) method more attractive, as it can also take into account the Breit operator and quantum electrodynamic (QED) effects [18,19] in the final RCI calculations, as the correlations considered in the RCI (RSMBPT) method also have their own matrix elements in the constructed RCI matrix, and therefore the Breit interaction and QED effects can be added in a regular way.

The MCDHF (RSMBPT) method is similar to the RCI (RSMBPT) method, but it is applied to the MCDHF calculation, i.e., instead of calculating the RCI, a matrix is constructed for the MCDHF calculation.

The papers [12–17] demonstrate how these methods work for a wide range of ions, both in terms of energy spectra and transition properties. They also provide a minimal but comprehensive set of Feynman diagrams for the GRASP package, describing all the most important and necessary CV, C, CC, and VV correlations based on RSMBPT theory. Each paper was devoted to a particular correlation type because the theory is quite complex; therefore, much work is needed to develop it, both in terms of obtaining expressions for Feynman diagrams in an irreducible tensorial form and in terms of reformulating them and, if that is not enough, to extend the library `librang` [20] in such a way that the spin-angular

theory [21,22] remains effective and known atomic symmetries (including the quasispin) are fully applied.

This paper extends the method, based on the stationary second-order Rayleigh–Schrödinger many-body perturbation theory in an irreducible tensorial form, developed by Gaigalas et al. [12–17]. It provides all the Feynman diagrams that describe CV, C, CC, and VV correlations for which analytical expressions are derived in an irreducible tensorial form and presents the general rules for obtaining algebraic expressions in an irreducible tensorial form for any Feynman diagram from the second-order perturbation theory. By generalizing the method developed in [12–17], this extension of the approach introduced in this paper reaches the next level of application for more general cases and essentially completes the methodology. It can be successfully applied in a similar way not only to other packages but also to the regular Rayleigh–Schrödinger many-body perturbation theory (the radial part of regular perturbation theory is, however, beyond the scope of the present paper) [23–25] and to the orthogonal operators [26]. This paper, together with the previous ones [12–17], provides a comprehensive representation of the newly developed version of the stationary second-order Rayleigh–Schrödinger many-body perturbation theory.

The paper consists of an introduction, four sections, a conclusion, and two appendices. Section 2 presents all the Feynman diagrams that describe correlations; these can be computed using the RSMBPT method developed in [12–17], and for these, analytical expressions are derived in an irreducible tensorial form. Section 3 presents the rules for getting algebraic expressions in an irreducible tensorial form for any Feynman diagram in *jj*-coupling of the stationary second-order Rayleigh–Schrödinger many-body perturbation theory [27]. Section 4 shows how the library `libracg` [20] is extended to calculate spin-angular parts of three-particle Feynman diagrams VV_3 and CV_7 [16,17]. Section 5 provides a test case that is directly derived from the paper's focus—the generalization and finalization of the methodology; therefore, it is intended to illustrate the RSMBPT approach's application at different stages of the calculation process (MCDHF and RCI). Conclusions are presented in Section 6.

2. Relativistic Second-Order Effective Hamiltonian of an Atom or Ion in Irreducible Tensorial Form for Including Correlations in the GRASP2018

The relativistic second-order effective Hamiltonian for an atom or ion, formulated in an irreducible tensorial form for the inclusion of correlations, is implemented in the new extended GRASP version, named GRASP2018_PT. This version builds upon the latest release of the GRASP package (GRASP2018) and the GRASPG [28,29]. GRASPG was applied because this program package allows the F, F', and G orbital sets to be easily distinguished during atomic data computations. It should be mentioned that extensions based on the theory detailed below can also be applied to older versions of the GRASP packages [2–5]. All the Feynman diagrams that describe a particular type of correlation are implemented in the GRASP2018_PT packages, as shown in Figure 1. Analytical expressions in irreducible tensorial form have been derived for them, and the appropriate software has been developed to calculate them. The analytical expressions of the diagrams are general and suitable for any atom or ion with any number of subshells in the configurations (including open subshells) and with any number of electrons in the subshells. Therefore, the developed methodology is general and can be applicable to any task and in any computational package.

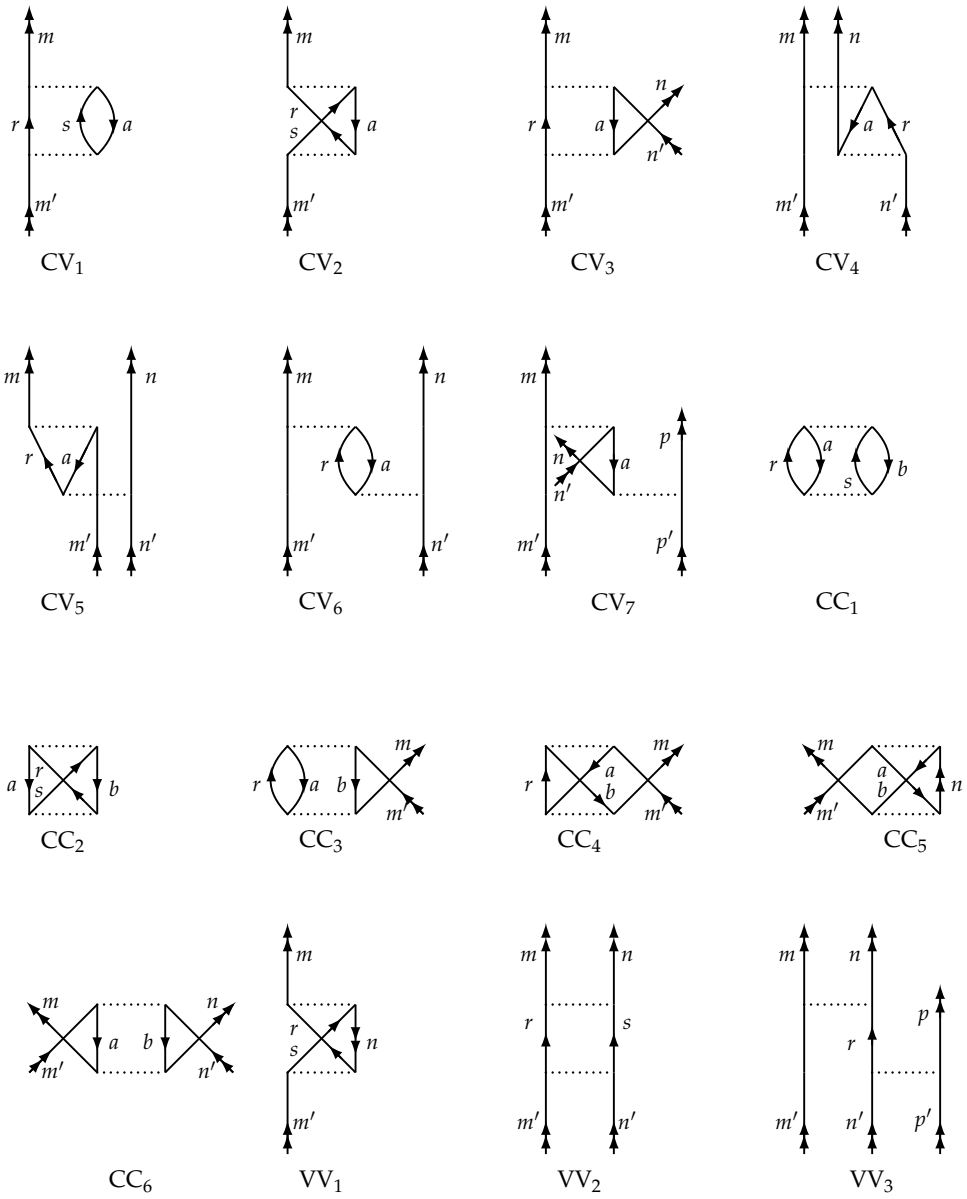

Figure 1. The Feynman diagrams of the second-order effective Hamiltonian that are included in the GRASP2018_PT computer package.

These diagrams can thus be used to assess the importance of the correlation configurations, in other words, to determine their correlation influence on the calculations. This includes single and double excitations attributed to CV, CC, C, and VV correlations. In Figure 1, all Feynman diagrams are grouped so that the most relevant and problematic correlations for RCI or MCDHF methods are mentioned before the others. The details of how this method is used and the results it is expected to produce are published in papers [12–17]. Analytical expressions for all these diagrams are also given in these papers.

2.1. Correlations Which Are Included in the Grasp2018_PT

In this section, we will present all the excitations (correlations) whose influence and importance the developed approach [12–17] allows to be identified by the RSMBPT method in advance of the RCI and MCDHF calculations. We will also list a few cases where correlations in the RCI and MCDHF methods need to be dealt with routinely.

2.1.1. Core–Valence Correlations

The first group of diagrams in Figure 1 includes Feynman diagrams that describe CV correlations. They are characterized by the fact that there must be one internal downward-directed line (core (hole) line) and at least two free double arrow lines (particle lines acting on valence subshells). This group includes diagrams CV_1, CV_2, CV_3, CV_4, CV_5, CV_6, and CV_7. CV_1 and CV_2 are one-particle; CV_3, CV_4, CV_5, and CV_6 are two-particle; and CV_7 is a three-particle diagram. Feynman diagram CV_1 describing correlations has the same influence on the relativistic configuration. Other diagrams affect both the configuration and its splitting. All of them can describe the four types of CV excitations (correlations) included in the GRASP2018_PT package. They are as follows:

- The first type:

$$(n_a\ell_a)\, j_a^{2j_a+1}\, (n_m\ell_m)\, j_m^{w_m} \rightarrow (n_a\ell_a)\, j_a^{2j_a}\, (n_m\ell_m)\, j_m^{w_m-1}\, (n_r\ell_r)\, j_r\, (n_s\ell_s)\, j_s \quad (1)$$

$$(n_a\ell_a)\, j_a^{2j_a+1}\, (n_m\ell_m)\, j_m^{w_m} \rightarrow (n_a\ell_a)\, j_a^{2j_a}\, (n_m\ell_m)\, j_m^{w_m-1}\, (n_s\ell_s)\, j_s^2 \quad (2)$$

- The second type:

$$(n_a\ell_a)\, j_a^{2j_a+1}\, (n_m\ell_m)\, j_m^{w_m}\, (n_n\ell_n)\, j_n^{w_n} \rightarrow (n_a\ell_a)\, j_a^{2j_a}\, (n_m\ell_m)\, j_m^{w_m-1}\, (n_n\ell_n)\, j_n^{w_n+1}\, (n_r\ell_r)\, j_r \quad (3)$$

- The third type:

$$(n_a\ell_a)\, j_a^{2j_a+1}\, (n_m\ell_m)\, j_m^{w_m}\, (n_n\ell_n)\, j_n^{w_n} \rightarrow (n_a\ell_a)\, j_a^{2j_a}\, (n_m\ell_m)\, j_m^{w_m-1}\, (n_n\ell_n)\, j_n^{w_n+2} \quad (4)$$

- The fourth type:

$$(n_a\ell_a)\, j_a^{2j_a+1}\, (n_m\ell_m)\, j_m^{w_m}\, (n_n\ell_n)\, j_n^{w_n}\, (n_p\ell_p)\, j_p^{w_p} \rightarrow (n_a\ell_a)\, j_a^{2j_a}\, (n_m\ell_m)\, j_m^{w_m-1}\, (n_n\ell_n)\, j_n^{w_n+1}\, (n_p\ell_p)\, j_p^{w_p+1}. \quad (5)$$

2.1.2. Core Correlations

C correlations are described by the same diagrams, CV_3, CV_4, CV_5, and CV_6, describing CV correlations. All open lines with double arrows act on the same valence subshell in this case. This leads to the type of C correlation that is included in this methodology:

- the first type:

$$(n_a\ell_a)\, j_a^{2j_a+1}\, (n_m\ell_m)\, j_m^{w_m} \rightarrow (n_a\ell_a)\, j_a^{2j_a}\, (n_m\ell_m)\, j_m^{w_m}\, (n_r\ell_r)\, j_r. \quad (6)$$

2.1.3. Core–Core Correlations

The second group of Feynman diagrams in Figure 1 describes the CC correlations. These diagrams are unique in that they have two internal downward-pointing lines (core (hole) lines). The remaining lines are the inner upward-pointing lines and/or the free double arrow lines. CC_1 and CC_2 are vacuum; CC_3, CC_4, and CC_5 are one-particle; and CC_6 is a two-particle diagram. Feynman diagrams CC_1 and CC_2 describing correlations have the same influence on the relativistic configuration. Other diagrams affect both the configuration and its splitting. All of them can describe the four types of CC excitations (correlations) included in the GRASP2018_PT package. They are as follows:

- The first type:

$$(n_a\ell_a)\, j_a^{2j_a+1}\, (n_b\ell_b)\, j_b^{2j_b+1}\, (n_m\ell_m)\, j_m^{w_m}\, (n_n\ell_n)\, j_n^{w_n} \rightarrow (n_a\ell_a)\, j_a^{2j_a}\, (n_b\ell_b)\, j_b^{2j_b}\, (n_m\ell_m)\, j_m^{w_m}\, (n_n\ell_n)\, j_n^{w_n}\, (n_r\ell_r)\, j_r\, (n_s\ell_s)\, j_s \quad (7)$$

$$(n_a\ell_a)\, j_a^{2j_a+1}\, (n_b\ell_b)\, j_b^{2j_b+1}\, (n_m\ell_m)\, j_m^{w_m}\, (n_n\ell_n)\, j_n^{w_n} \rightarrow (n_a\ell_a)\, j_a^{2j_a}\, (n_b\ell_b)\, j_b^{2j_b}\, (n_m\ell_m)\, j_m^{w_m}\, (n_n\ell_n)\, j_n^{w_n}\, (n_r\ell_r)\, j_r^2 \quad (8)$$

$$(n_a\ell_a)\, j_a^{2j_a+1} (n_m\ell_m)\, j_m^{w_m}\, (n_n\ell_n)\, j_n^{w_n} \rightarrow (n_a\ell_a)\, j_a^{2j_a-1}\, (n_m\ell_m)\, j_m^{w_m}\, (n_n\ell_n)\, j_n^{w_n}\, (n_r\ell_r)\, j_r\, (n_s\ell_s)\, j_s \quad (9)$$

$$(n_a\ell_a)\, j_a^{2j_a+1} (n_m\ell_m)\, j_m^{w_m}\, (n_n\ell_n)\, j_n^{w_n} \rightarrow (n_a\ell_a)\, j_a^{2j_a-1}\, (n_m\ell_m)\, j_m^{w_m}\, (n_n\ell_n)\, j_n^{w_n}\, (n_r\ell_r)\, j_r^2 \quad (10)$$

- The second type:

$$(n_a\ell_a)\, j_a^{2j_a+1}\, (n_b\ell_b)\, j_b^{2j_b+1}\, (n_m\ell_m)\, j_m^{w_m}\, (n_n\ell_n)\, j_n^{w_n} \rightarrow (n_a\ell_a)\, j_a^{2j_a}\, (n_b\ell_b)\, j_b^{2j_b}\, (n_m\ell_m)\, j_m^{w_m+1}\, (n_n\ell_n)\, j_n^{w_n}\, (n_r\ell_r)\, j_r \quad (11)$$

$$(n_a\ell_a)\, j_a^{2j_a+1}\, (n_m\ell_m)\, j_m^{w_m}\, (n_n\ell_n)\, j_n^{w_n} \rightarrow (n_a\ell_a)\, j_a^{2j_a-1}\, (n_m\ell_m)\, j_m^{w_m+1}\, (n_n\ell_n)\, j_n^{w_n}\, (n_r\ell_r)\, j_r \quad (12)$$

- The third type:

$$(n_a\ell_a)\, j_a^{2j_a+1}\, (n_b\ell_b)\, j_b^{2j_b+1}\, (n_m\ell_m)\, j_m^{w_m}\, (n_n\ell_n)\, j_n^{w_n} \rightarrow (n_a\ell_a)\, j_a^{2j_a}\, (n_b\ell_b)\, j_b^{2j_b}\, (n_m\ell_m)\, j_m^{w_m+2}\, (n_n\ell_n)\, j_n^{w_n} \quad (13)$$

$$(n_a\ell_a)\, j_a^{2j_a+1}\, (n_m\ell_m)\, j_m^{w_m}\, (n_n\ell_n)\, j_n^{w_n} \rightarrow (n_a\ell_a)\, j_a^{2j_a-1}\, (n_m\ell_m)\, j_m^{w_m+2}\, (n_n\ell_n)\, j_n^{w_n} \quad (14)$$

- The fourth type:

$$(n_a\ell_a)\, j_a^{2j_a+1}\, (n_b\ell_b)\, j_b^{2j_b+1}\, (n_m\ell_m)\, j_m^{w_m}\, (n_n\ell_n)\, j_n^{w_n} \rightarrow (n_a\ell_a)\, j_a^{2j_a}\, (n_b\ell_b)\, j_b^{2j_b}\, (n_m\ell_m)\, j_m^{w_m+1}\, (n_n\ell_n)\, j_n^{w_n+1} \quad (15)$$

$$(n_a\ell_a)\, j_a^{2j_a+1}\, (n_m\ell_m)\, j_m^{w_m}\, (n_n\ell_n)\, j_n^{w_n} \rightarrow (n_a\ell_a)\, j_a^{2j_a-1}\, (n_m\ell_m)\, j_m^{w_m+1}\, (n_n\ell_n)\, j_n^{w_n+1}. \quad (16)$$

2.1.4. Valence–Valence Correlations

The third group of Feynman diagrams in Figure 1 describes VV correlations. These diagrams are unique in that they have at least one internal upward-directed line (particle line acting on virtual orbitals). The remaining lines are the double arrow lines (particle lines acting on valence subshells). VV_1 is a one-particle diagram, VV_2 is a two-particle diagram, and VV_3 is a three-particle diagram. All of them can describe the four types of VV excitations (correlations) included in the GRASP2018_PT package. They are as follows:

- The first type:

$$(n_m\ell_m)\, j_m^{w_m}\, (n_n\ell_n)\, j_n^{w_n} \rightarrow (n_m\ell_m)\, j_m^{w_m-2}\, (n_n\ell_n)\, j_n^{w_n}\, (n_r\ell_r)\, j_r\, (n_s\ell_s)\, j_s \quad (17)$$

$$(n_m\ell_m)\, j_m^{w_m}\, (n_n\ell_n)\, j_n^{w_n} \rightarrow (n_m\ell_m)\, j_m^{w_m-2}\, (n_n\ell_n)\, j_n^{w_n}\, (n_s\ell_s)\, j_s^2 \quad (18)$$

- The second type:

$$(n_m\ell_m)\, j_m^{w_m}\, (n_n\ell_n)\, j_n^{w_n} \rightarrow (n_m\ell_m)\, j_m^{w_m-1}\, (n_n\ell_n)\, j_n^{w_n-1}\, (n_r\ell_r)\, j_r\, (n_s\ell_s)\, j_s \quad (19)$$

$$(n_m\ell_m)\, j_m^{w_m}\, (n_n\ell_n)\, j_n^{w_n} \rightarrow (n_m\ell_m)\, j_m^{w_m-1}\, (n_n\ell_n)\, j_n^{w_n-1}\, (n_s\ell_s)\, j_s^2 \quad (20)$$

- The third type:

$$(n_m\ell_m)\, j_m^{w_m}\, (n_n\ell_n)\, j_n^{w_n} \rightarrow (n_m\ell_m)\, j_m^{w_m+1}\, (n_n\ell_n)\, j_n^{w_n-2}\, (n_r\ell_r)\, j_r \quad (21)$$

- The fourth type:

$$(n_m\ell_m)\, j_m^{w_m}\, (n_n\ell_n)\, j_n^{w_n}\, (n_p\ell_p)\, j_p^{w_p} \rightarrow (n_m\ell_m)\, j_m^{w_m+1}\, (n_n\ell_n)\, j_n^{w_n-1}\, (n_p\ell_p)\, j_p^{w_p-1}\, (n_r\ell_r)\, j_r. \quad (22)$$

2.1.5. Contributions of RSMBPT to Off-Diagonal Matrix Elements

The following are contributions of RSMBPT to off-diagonal $\left\langle (n_m\ell_m)\, j_m^{w_m}\, (n_n\ell_n)\, j_n^{w_n} \right\| \widehat{\mathcal{H}}^{(2)}_{Effective} \left\| (n_m\ell_m)\, j_m^{w_m-2}\, (n_n\ell_n)\, j_n^{w_n+2} \right\rangle$ matrix elements:

- The second type of core–valence correlations

$$(n_a\ell_a)\, j_a^{2j_a+1}\, (n_m\ell_m)\, j_m^{w_m}\, (n_n\ell_n)\, j_n^{w_n} \rightarrow (n_a\ell_a)\, j_a^{2j_a}\, (n_m\ell_m)\, j_m^{w_m-1}\, (n_n\ell_n)\, j_n^{w_n+1}\, (n_r\ell_r)\, j_r. \quad (23)$$

This type of correlation is described by two-particle Feynman diagrams CV_3, CV_4, CV_5, and CV_6.

- The third type of core–core correlations

$$(n_a\ell_a)\, j_a^{2j_a+1}\, (n_b\ell_b)\, j_b^{2j_b+1}\, (n_m\ell_m)\, j_m^{w_m}\, (n_n\ell_n)\, j_n^{w_n} \rightarrow (n_a\ell_a)\, j_a^{2j_a}\, (n_b\ell_b)\, j_b^{2j_b}\, (n_m\ell_m)\, j_m^{w_m}\, (n_n\ell_n)\, j_n^{w_n+2}. \quad (24)$$

This type of correlation is described by the two-particle Feynman diagram CC_6.

- The first type of valence–valence correlations

$$(n_m\ell_m)\, j_m^{w_m}\, (n_n\ell_n)\, j_n^{w_n} \rightarrow (n_m\ell_m)\, j_m^{w_m-2}\, (n_n\ell_n)\, j_n^{w_n}\, (n_r\ell_r)\, j_r\, (n_s\ell_s)\, j_s. \quad (25)$$

This type of correlation is described by the two-particle Feynman diagram VV_2.

2.2. Correlations That Are Not Included in the Grasp2018_PT

The following correlations are not included in the GRASP2018_PT program:

- Valence correlations

$$(n_m\ell_m)\, j_m^{w_m} \rightarrow (n_m\ell_m)\, j_m^{w_m-1}\, (n_r\ell_r)\, j_r \quad (26)$$

- Core correlations

$$(n_a\ell_a)\, j_a^{2j_a+1}\, (n_m\ell_m)\, j_m^{w_m} \rightarrow (n_a\ell_a)\, j_a^{2j_a}\, (n_m\ell_m)\, j_m^{w_m+1}. \quad (27)$$

The above excitations shall be calculated in the regular way as before in the GRASP2018 package.

2.3. Multireference Space

The choice of multireference (MR) space for the Rayleigh–Schrödinger many-body perturbation theory (*P*-space according to many-body perturbation theory [23]) is the same as for the ordinary calculation of the GRASP2018 [12]. The simplest way to construct an MR is to include in the MR only those CSFs for which the eigenvalue problem is solvable. But in general, the choice of the MR space is an important and responsible task in the search for accurate atomic characteristics. Often, the MR space is extended so that the CSFs in the MR are those that can be formed from nearly degenerate configurations [7,30] (see chapter 4 in [30]). Thus, although in the RSMBPT theory we only consider single and double excitations, it can also be considered to include the most important excitations higher than double excitations when, in the MR space, to the CSFs for which eigenvalues are searched for, we add the CSFs for which eigenvalues are not searched for but are only included for correlations in single and double excitations.

The wave function based on the CSFs in the MR is the first approximation, and it is the starting point for further refinements. So the selection of the MR in advance or *a priori* is far from trivial, and it often requires a number of exploratory calculations to find a good MR. For details on how the MR space in RSMBPT theory is selected in the calculations, see the papers [12–17].

3. The Rules for Getting Algebraic Expressions in an Irreducible Tensorial Form of Feynman Diagrams

In this section, we give the rules for finding the algebraic expressions of the tensorial form of any linked-cluster Feynman diagrams. We analyze the Feynman diagrams of the second order of the effective operator of perturbation theory, describing the Coulomb interaction in the relativistic atomic theory. These rules are similar to those in the non-relativistic theory of the atom [27]. They are formulated on the basis of Wick's theorem in coupled tensorial form [27,31] and the experience accumulated in previous research [12–16]. Using these rules, we easily obtain all algebraic expressions for the Feynman diagrams coming into the second order of perturbation theory in an irreducible tensorial form. These rules are as follows:

1. The sum of the sets of quantum numbers n, l, j describing all electron lines and the ranks k describing all interaction (horizontal) lines is obtained. For example, for the diagram CV_7 from Figures 1 and 2, we have $\sum\limits_{m,m'}\sum\limits_{n,n'}\sum\limits_{p,p'}\sum\limits_{k,k'}$.

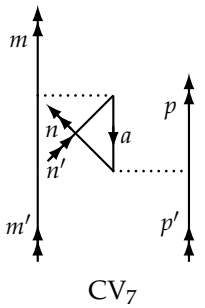

CV_7

$$= -\sum_{k,k',x}\sqrt{\frac{[x]}{[k,k']}}\sum_{m,m'}\sum_{n,n'}\sum_{p,p'}$$
$$\times\left[\left[\left[\,a^{(j_m)}\times\tilde{a}^{(j_{m'})}\,\right]^{(k)}\times\left[\,\tilde{a}^{(j_{n'})}\times a^{(j_n)}\,\right]^{(x)}\right]^{(k')}\times\left[\,a^{(j_p)}\times\tilde{a}^{(j_{p'})}\,\right]^{(k')}\right]^{(0)}$$
$$\times\sum_{a}\frac{1}{\left(\varepsilon_a+\varepsilon_{p'}-\varepsilon_n-\varepsilon_p\right)}\begin{Bmatrix} j_n & j_{n'} & x\\ k & k' & j_a\end{Bmatrix}X_k(ma,m'n')\;X_{k'}(np,a\;p')$$

Figure 2. The CV Feynman diagram of the second-order effective Hamiltonian for the third and fourth types of core–valence correlations $(n_a\ell_a)\,j_a^{2j_a+1}\,(n_m\ell_m)\,j_m^{w_m}\,(n_n\ell_n)\,j_n^{w_n}\;\rightarrow\;(n_a\ell_a)\,j_a^{2j_a}\;\;(n_m\ell_m)\,j_m^{w_m-1}\,(n_n\ell_n)\,j_n^{w_n+2}$ and $(n_a\ell_a)\,j_a^{2j_a+1}\,(n_m\ell_m)\,j_m^{w_m}\,(n_n\ell_n)\,j_n^{w_n}\,(n_p\ell_p)\,j_p^{w_p}\;\rightarrow\;(n_a\ell_a)\,j_a^{2j_a}\,(n_m\ell_m)\,j_m^{w_m-1}\,(n_n\ell_n)\,j_n^{w_n+1}\,(n_p\ell_p)\,j_p^{w_p+1}$.

2. A matrix element is assigned for each Coulomb interaction line (horizontal Feynman diagram line):
$$\frac{1}{\sqrt{[k]}}\ X_k(ij, i'j').$$
For the diagram CV_7, we have $\frac{1}{\sqrt{[k,k']}}\ X_k(ma, m'n')\ X_{k'}(np, a\ p')$.
3. The phase multiplier
$$(-1)^{a+c+h}$$
is assigned to the whole diagram, where a is the number of $\left[\tilde{a}^{(j)} \times a^{(j')}\right]^{(k)}$ pairs, where the annihilation operator of the secondary quantization is first and the creation operator is second in the diagram (to find out how, see rule 6.2.2. below); c is the number of closed loops of the electron line in the diagram; and h is the number of internal hole lines and internal lines with double arrows pointing downward. For example, for the diagram CV_7, we have $a = 1$, $c = 1$, and $h = 0$.
4. The whole chart corresponds to a weighted multiplier of
$$\frac{1}{\lambda}.$$
For diagrams without internal double arrow lines, $\lambda = 2$ if the diagram is symmetrical (replacing all its vertices with respect to the line of interaction results in a typologically identical diagram), and if not, $\lambda = 1$. For diagrams with internal double arrows, $\frac{1}{\lambda}$ is equal to the weighted multiplier of the diagram obtained by disconnecting the double arrows. For the diagram CV_7, we have $\lambda = 1$.
5. The lower horizontal interaction line of the diagram corresponds to the energy multiplier
$$\frac{1}{D}, \tag{28}$$
where $D = \sum(\varepsilon_{\text{down}} - \varepsilon_{\text{up}})$ is an energy denominator and $\varepsilon_{\text{down}}$ (ε_{up}) is the single-particle eigenvalue associated with the down- (up-) orbital lines to (from) the lowest interaction line of the diagram. For the diagram CV_7, we have $D = \left(\varepsilon_a + \varepsilon_{p'} - \varepsilon_n - \varepsilon_p\right)$. This rule is the same as Goldstone evaluation rules [32] (see, for example, rule c on page 265 [23]).
6. The Feynman diagram has an irreducible tensorial form of operators of second quantization, which can be found using the graphical representation of the angular momentum technique [27,33,34] by applying the rules below:
    - 6.1 The diagram of angular momentum typologically equivalent to the initial Feynman one is drawn (for example, the diagram A_1 of angular momentum for Feynman diagram CV_7 from Figures 1 and 2 is shown in Figure 3), where
        - 6.1.1 Free lines A_2 or A_4 (see Figure 4) from the Feynman diagram are replaced by graphic elements A_3 or A_5 in the angular momentum diagram, shown in Figure 4. The diagram A_3 represents the creation operator in the angular momentum diagram, and A_5 represents the annihilation operator.
        - 6.1.2 Internal electronic lines are carried over unchanged.
        - 6.1.3 The horizontal lines A_6 (see Figure 5) corresponding to the interactions in the Feynman diagram are replaced by the graphical elements A_7 presented in Figure 5. The diagram A_7 shows the angular momentum line corresponding to the rank (k or k') of the Coulomb interaction in the angular momentum diagram.

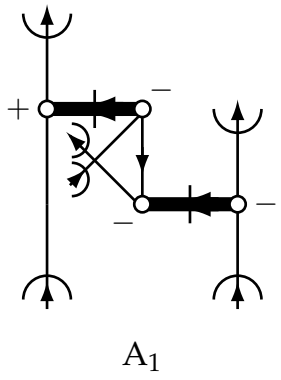

Figure 3. The diagram of angular momentum for Feynman diagram CV_7 from Figure 2.

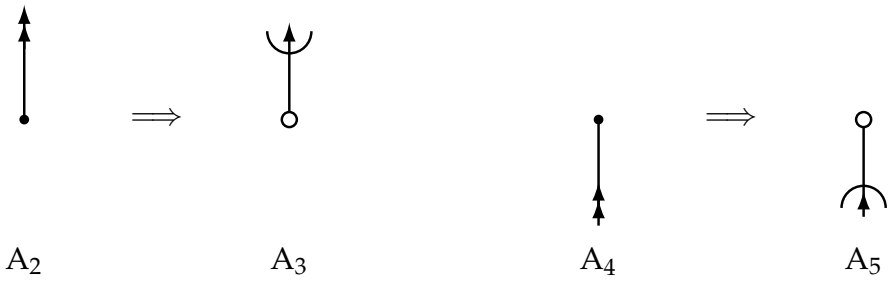

Figure 4. The free lines A_2 or A_4 from the Feynman diagram are replaced by graphic elements A_3 or A_5 in angular momentum diagram, respectively.

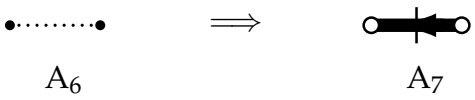

Figure 5. The horizontal lines A_6 corresponding to the interactions of the Feynman diagram are replaced by the graphical elements A_7 in the angular momentum diagram.

6.1.4 Nodes without signs are provided with a "+" sign if the line with an arrow coming out of the node can be turned counterclockwise to align it with the line having an arrow entering the node without crossing the thickened line (see A_8 in Figure 6); otherwise, the node is given the sign "−" (see A_9 in Figure 6).

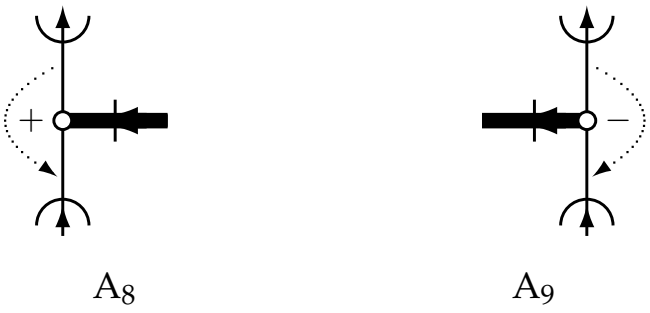

Figure 6. An illustration of the 6.1.4 rule for determining the signs at the vertex of the angular momentum diagram.

6.2 The obtained recoupling diagram and tensorial product of operators of second quantization from the diagram of angular momentum (for example, from the A_1, see Figure 3):

6.2.1 The lines related to the secondary quantization operators need to be cut.

6.2.2 Then, through the diagram depicting the generalized Clebsch–Gordan coefficient, the graphical elements representing the secondary quantization operators are connected into pairs, and the pairs—successively from left to right—into the resulting rank [27,31]. In a pair, the first is the creation operator, and if the pair consists of operators connected in the Feynman diagram by internal electron lines, then the first is the operator belonging to the leftmost upper node. This yields a graphical representation of the irreducible tensorial product of operators of the second quantization. For example, we obtain diagram A_{10} (see Figure 7), representing the tensorial product of the second quantization operators for Feynman diagram A_1 (see Figure 3), with the additional summations $\sum_{J_1,J_2,J}$ according to [27,33,34].

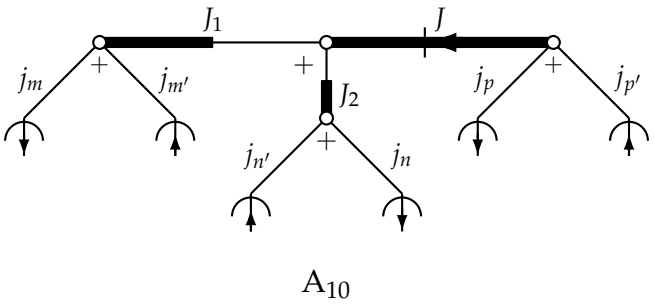

Figure 7. The graphical representation of the irreducible tensorial product of second-quantization operators A_{10} corresponding to Feynman diagram CV_7.

6.2.3 The parts of the original diagram remaining after cutting are closed up according to the graphical technique developed in [27,31,33,34] by the same generalized Clebsch–Gordan coefficient as the irreducible tensorial product. As a result, we obtain the recouping matrix, which can be expressed through the $3nj$-coefficients by using [27,33,34]. For example, by applying this rule, we get the recouping matrix A_{11} in graphical representation (see Figure 8) for Feynman diagram CV_7.

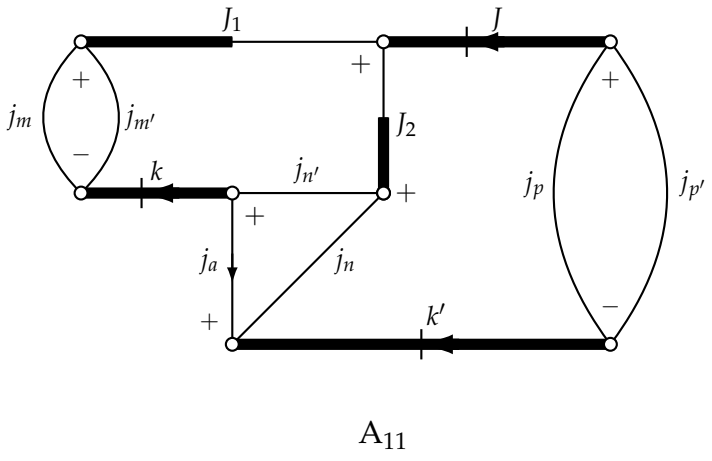

Figure 8. The recoupling matrix for Feynman diagram CV_7 from Figure 2.

So, using all these rules, we first obtain all the necessary multipliers (including the phase multiplier) and the tensorial product and the recoupling matrix, both of which are represented by the graphical technique of angular momentum [27,33,34]. Then we already

have the tensorial form of the Feynman diagram, which is partly expressed in algebraic terms and partly represented graphically. To get the full expression in algebraic form, further steps are required.

So, secondly, the tensorial product can easily be rewritten from the graphical form into the normal (algebraic) form by using [27,33,34]. For example, the tensorial product shown in A_{10} has the following tensorial product:

$$A_{10} = \left[\left[\left[a^{(j_m)} \times \tilde{a}^{(j_{m'})} \right]^{(J_1)} \times \left[\tilde{a}^{(j_{n'})} \times a^{(j_n)} \right]^{(J_2)} \right]^{(J)} \times \left[a^{(j_p)} \times \tilde{a}^{(j_{p'})} \right]^{(J)} \right]^{(0)}. \quad (29)$$

Thirdly, the algebraic expression for the recoupling matrix is obtained by following the necessary steps of the graphical momentum theory [27,33,34]. For example, after the transformations of the recoupling matrix A_{11} (such as removing the arrows on the lines (lines j_a, J, k, and k'), removing a swipe from the lines (lines J, k, and k'), cutting the diagram in two lines (lines J_1, k and lines J, k'), changing the signs at nodes (vertices), and rearranging the thick and semi-thick lines), we get the following algebraic expression:

$$A_{11} = -\sqrt{[J_2]} \begin{Bmatrix} j_n & j_{n'} & J_2 \\ k & k' & j_a \end{Bmatrix} \delta(J_1, k)\, \delta(J, k'). \quad (30)$$

Thus, taking into account all these rules (1–6.2.3) and the above transformations (all three steps), we obtain the final expression of the Feynman diagram CV_7 shown in Figure 2.

Based on these rules and transformations, it is possible to obtain all the expressions for the Feynman diagrams of Coulomb interaction coming into the second-order expansion of the perturbation theory of the effective operator in irreducible tensorial form. At the same time, it is possible to obtain analytical expressions for all the Feynman diagrams that have been dealt with in the previous papers [12–16].

We also want to point out that the reason we use here the graphical version of the Jucys, Bandzaitis, and Gaigalas momentum theory [27,31,33,34] is that it is the most appropriate of all the available graphical methods for representing the secondary quantization operators in the irreducible tensorial form and for all the necessary operations on them (operators) [34]. This greatly facilitates finding all the necessary expressions for Feynman diagrams in the irreducible tensorial form in both non-relativistic atomic theory [27] and relativistic atomic theory [12–16].

4. The Spin-Angular Integration for Second-Order Feynman Diagrams in an Irreducible Tensorial Form

In the development of this methodology [12–17], all the necessary expressions for the Feynman diagrams from Figure 1 were first obtained in irreducible tensorial form. This makes it possible, as shown in previous articles, for the contribution deriving from the CV, C, CC, and VV correlations of the configurations K' to $E(K\chi J)$ in the second order of the perturbation theory to be expressed as

$$
\begin{aligned}
&\Delta E_{PT(\mathrm{CV,C,CC,VV})} \\
&\quad = \Delta\mathcal{E}_{0\ PT(\mathrm{CV,C,CC,VV})}(KJ) \\
&\quad + \sum_{n\ell j}\sum_{k>0} \widetilde{f}_k(\ell j^w,\ K\chi J)\ \Delta\mathcal{F}^k_{PT(\mathrm{CV,C,CC,VV})}(n\ell j,\ n\ell j) \\
&\quad + \sum_{n\ell j}\sum_{n'\ell'j'>n\ell j}\left\{\sum_{k>0}\widetilde{f}_k\left(\ell j^w\ \ell' j'^{w'},\ K\chi J\right)\Delta\mathcal{F}^k_{PT(\mathrm{CV,CC,VV})}(n\ell j,\ n'\ell' j') \right. \\
&\quad + \sum_k \widetilde{g}_k\left(\ell j^w\ \ell' j'^{w'},\ K\chi J\right)\Delta\mathcal{G}^k_{PT(\mathrm{CV,CC,VV})}(n\ell j,\ n'\ell' j') \\
&\quad \left. + \sum_k \widetilde{v}_k\left(\ell j^w\ \ell' j'^{w'}, \ell j^{w-2}\ \ell' j'^{w'+2},\ K\chi J\ K'\chi' J\right)\Delta\mathcal{R}^k_{PT(\mathrm{CV,CC,VV})}(n\ell jn\ell j,\ n'\ell' j'n'\ell' j')\right\} \\
&\quad + \sum_{\substack{n\ell j \\ n'\ell' j'\neq n\ell j}}\ \sum_{\substack{k>0 \\ k',x}}\left\langle\Psi\middle\|\left[\left[\tilde{a}^{(j)}\times a^{(j)}\right]^{(k)}\times\left[\left[a^{(j')}\times\tilde{a}^{(j')}\right]^{(x)}\times\left[a^{(j')}\times\tilde{a}^{(j')}\right]^{(k')}\right]^{(k)}\right]^{(0)}\middle\|\Psi\right\rangle \\
&\qquad \times \Delta\widetilde{\mathcal{R}}^{(k,k',x)}_{PT(\mathrm{VV})}(n\ell j\ n'\ell' j'\ n'\ell' j') \\
&\quad + \sum_{\substack{n\ell j \\ n'\ell' j'\neq n\ell j \\ n''\ell'' j''\neq n\ell j}}\ \sum_{\substack{k>0 \\ k',x}}\left\langle\Psi\middle\|\left[\left[\left[\tilde{a}^{(j)}\times a^{(j)}\right]^{(k)}\times\left[a^{(j'')}\times\tilde{a}^{(j'')}\right]^{(x)}\right]^{(k')}\times\left[a^{(j')}\times\tilde{a}^{(j')}\right]^{(k')}\right]^{(0)}\middle\|\Psi\right\rangle \\
&\qquad \times \Delta\widetilde{\mathcal{R}}^{(k,k',x)}_{PT(\mathrm{VV})}(n\ell j\ n'\ell' j'\ n''\ell'' j'') \\
&\quad + \sum_{\substack{n\ell j \\ n'\ell' j'\neq n\ell j}}\ \sum_{\substack{k>0 \\ k',x}}\left\langle\Psi\middle\|\left[\left[a^{(j)}\times\tilde{a}^{(j)}\right]^{(k)}\times\left[\left[a^{(j')}\times\tilde{a}^{(j')}\right]^{(x)}\times\left[\tilde{a}^{(j')}\times a^{(j')}\right]^{(k')}\right]^{(k)}\right]^{(0)}\middle\|\Psi\right\rangle \\
&\qquad \times \Delta\widetilde{\widetilde{\mathcal{R}}}^{(k,k',x)}_{PT(\mathrm{CV})}(n\ell j\ n'\ell' j'\ n'\ell' j') \\
&\quad + \sum_{\substack{n\ell j \\ n'\ell' j'\neq n\ell j \\ n''\ell'' j''\neq n\ell j}}\ \sum_{\substack{k>0 \\ k',x}}\left\langle\Psi\middle\|\left[\left[\left[a^{(j)}\times\tilde{a}^{(j)}\right]^{(k)}\times\left[\tilde{a}^{(j'')}\times a^{(j'')}\right]^{(x)}\right]^{(k')}\times\left[\tilde{a}^{(j')}\times a^{(j')}\right]^{(k')}\right]^{(0)}\middle\|\Psi\right\rangle \\
&\qquad \times \Delta\widetilde{\widetilde{\mathcal{R}}}^{(k,k',x)}_{PT(\mathrm{CV})}(n\ell j\ n'\ell' j'\ n''\ell'' j''),
\end{aligned}
\tag{31}
$$

where $\langle\ \Psi\ \|$ and $\|\ \Psi\ \rangle$ are configuration state functions, meanwhile $\widetilde{f}_k(...)$, $\widetilde{g}_k\left(\ell j^w\ \ell' j'^{w'},\ K\chi J\right)$, and $\widetilde{v}_k\left(\ell j^w\ \ell' j'^{w'}, \ell j^{w-2}\ \ell' j'^{w'+2},\ K\chi J\ K'\chi' J\right)$, respectively, are spin-angular coefficients f_{abk}, g_{abk} (see (87) in [7]), and $v^{\alpha\beta}_{abcd;k}$ (see (34) in [20]) from which submatrix elements $\left\langle \ell j\middle\| C^{(k)}\middle\|\ell' j'\right\rangle$ are extracted. Therefore, summation over k runs over all possible values instead of the values that satisfy the triangular condition $(\ell\ell' k)$ as it is in the regular case and these coefficients $\left\langle \ell j\middle\| C^{(k)}\middle\|\ell' j'\right\rangle$ are themselves included in $\Delta\mathcal{F}^k_{PT(\mathrm{CV,C,CC,VV})}(n\ell j,\ n\ell j)$, $\Delta\mathcal{F}^k_{PT(\mathrm{CV,CC,VV})}(n\ell j,\ n'\ell' j')$, $\Delta\mathcal{G}^k_{PT(\mathrm{CV,CC,VV})}(n\ell j,\ n'\ell' j')$, $\Delta\mathcal{R}^k_{PT(\mathrm{CV,CC,VV})}(n\ell jn\ell j,\ n'\ell' j'n'\ell' j')$, $\Delta\widetilde{\mathcal{R}}^{(k,k',x)}_{PT(\mathrm{VV})}(n\ell j\ n'\ell' j'\ n'\ell' j')$, $\Delta\widetilde{\mathcal{R}}^{(k,k',x)}_{PT(\mathrm{VV})}(n\ell j\ n'\ell' j'\ n''\ell'' j'')$, $\Delta\widetilde{\widetilde{\mathcal{R}}}^{(k,k',x)}_{PT(\mathrm{CV})}(n\ell j\ n'\ell' j'\ n'\ell' j')$, and $\Delta\widetilde{\widetilde{\mathcal{R}}}^{(k,k',x)}_{PT(\mathrm{CV})}(n\ell j\ n'\ell' j'\ n''\ell'' j'')$. These latter coefficients are the amplitude of second-order effective operator form Rayleigh–Schrödinger many-body perturbation theory [23,35] according to terminology [27] or effective interaction strength according to terminology [19].

They are proportional to Slater integrals with some additional coefficients, such as simple multipliers and/or 6j-coefficients.

As shown in (31), the order in which the ranks are combined into a tensorial product varies. The tensorial structure of the triple tensor in the first reduced matrix element shows that the rank x (coming from the second pair of operators of second quantization) and the rank k' (coming from the third pair of operators of second quantization) are coupled into the rank k, and the rank k (coming from the first pair of operators of second quantization) is coupled with the rank k from the previous coupling into the final rank 0. The tensorial structure of the triple tensor in the second reduced matrix element shows that the rank k (coming from the first pair of operators of second quantization) and rank x (coming from the second pair of operators of second quantization) are coupled into the rank k', and the latter and rank k' (coming from the third pair of operators of second quantization) are coupled into the final rank 0. The similar structure of triple tensors we have and, for the rest, reduced matrix elements. The notations of the ranks k, k', and x in tensorial products correspond to the symmetry of the formula, i.e., the notation of the rank k indicates that its values are determined by the permissible values of the $\left\langle \ell j \middle\| C^{(k)} \middle\| \ell' j' \right\rangle$ coefficients, where the coefficients themselves belong to the top interaction line of the Feynman diagram, whereas the notation of the rank k' indicates that its values are determined by the $\left\langle \ell j \middle\| C^{(k)} \middle\| \ell' j' \right\rangle$ coefficients coming from the lower interaction line of the Feynman diagram. Meanwhile, the notation x indicates that its values are not controlled by the aforementioned coefficients but are determined by the corresponding ranks of the secondary quantization operators. These notations make it easier to understand the formula itself and to implement it programmatically. As we can see, the pair of secondary quantization operators with the ranks j is always coupled into the rank k, and the rightmost pair of the operators with the ranks j' is coupled into k'. Since Formula (31) is applicable to various cases, its tensorial structure varies, as it is optimized for each specific case under consideration so that the spin-angular method [21,22], which is based on the Racah algebra in the two spaces j, q, can be fully utilized.

The contribution of the CV, C, CC, and VV correlations in the second order of the perturbation theory is expressed over the corresponding spin-angular part (with multiplication, except for $\Delta\mathcal{E}_{0\ PT(\mathrm{CV,C,CC,VV})}(KJ)$):

- $\Delta\mathcal{E}_{0\ PT(\mathrm{CV,C,CC,VV})}(KJ)$ for CV [12,17], C [13], CC [14], and VV [15,16] correlations;
- $\Delta\mathcal{F}^{k}_{PT(\mathrm{CV,C,CC,VV})}(n\ell j,\ n\ell j)$ for CV [12,17], C [13], CC [14], and VV [15,16] correlations;
- $\Delta\mathcal{F}^{k}_{PT(\mathrm{CV,CC,VV})}(n\ell j,\ n'\ell' j')$ for CV [12,17], CC [14], and VV [15,16] correlations;
- $\Delta\mathcal{G}^{k}_{PT(\mathrm{CV,CC,VV})}(n\ell j,\ n'\ell' j')$ for CV [12], CC [14], and VV [15] correlations;
- $\Delta\mathcal{R}^{k}_{PT(\mathrm{CV,CC,VV})}(n\ell jn\ell j,\ n'\ell' j'n'\ell' j')$ for CV [12], CC [14], and VV [15] correlations;
- $\Delta\widetilde{\mathcal{R}}^{(k,k',x)}_{PT(\mathrm{VV})}(n\ell j\ n'\ell' j'\ n'\ell' j')$ for VV correlations [16];
- $\Delta\widetilde{\mathcal{R}}^{(k,k',x)}_{PT(\mathrm{VV})}(n\ell j\ n'\ell' j'\ n''\ell'' j'')$ for VV correlations [16];
- $\Delta\widetilde{\widetilde{\mathcal{R}}}^{(k,k',x)}_{PT(\mathrm{CV})}(n\ell j\ n'\ell' j'\ n'\ell' j')$ for CV correlations [17];
- $\Delta\widetilde{\widetilde{\mathcal{R}}}^{(k,k',x)}_{PT(\mathrm{CV})}(n\ell j\ n'\ell' j'\ n''\ell'' j'')$ for CV correlations [17].

Expressions for the member $\Delta\mathcal{R}^{k}_{PT(\mathrm{CV,CC,VV})}(n\ell jn\ell j,\ n'\ell' j'n'\ell' j')$ is coming only from the off-diagonal matrix element for accounting for CV (23), CC (24), and VV (25) correlations, while the expressions for the remaining parts come only from the diagonal matrix elements for accounting for the rest of the correlations [12–17]. It should be noted that the $\Delta\mathcal{R}^{k}_{PT(\mathrm{CV,CC,VV})}(n\ell jn\ell j,\ n'\ell' j'n'\ell' j')$ factors are not included in the RCI (RSMBPT) computations [12–17]. They are only considered in the RCI+RSMBPT calculations [12].

The specificity and advantage of this approach [12–17] is that the spin-angular parts of vacuum diagrams CC_1 and CC_2 from Figure 1 are proportional to the simple multiplier and the spin-angular parts of one-particle Feynman diagrams (CV_1, CV_2, CC_3, CC_4, CC_5, and VV_1 from Figure 1) are proportional to the number of subshell occupation, while the spin-angular parts $\widetilde{f}_k(\ell j^w,\ K\chi J)$, $\widetilde{f}_k\left(\ell j^w\ \ell' j'^{w'},\ K\chi J\right)$, $\widetilde{g}_k\left(\ell j^w\ \ell' j'^{w'},\ K\chi J\right)$, and $\widetilde{v}_k\left(\ell j^w\ \ell' j'^{w'}, \ell j^{w-2}\ \ell' j'^{w'+2},\ K\chi J\ K'\chi' J\right)$ of two-particle Feynman diagrams (CV_3, CV_4, CV_5, CV_6, CC_6, and VV_2 from Figure 1) can be found using a standard library `librang` [20] from the GRASP2018 [6]. In addition, the spin-angular part of the vacuum and one-particle Feynman diagrams are independent of the term. Meanwhile, the spin-angular coefficients of the three-particle diagrams CV_7 and VV_3 from Figure 1 are also partly calculated with the help of these libraries. These would be coefficients $\widetilde{f}_k(\ell j^w,\ K\chi J))$ and $\widetilde{f}_k\left(\ell j^w\ \ell' j'^{w'},\ K\chi J\right)$. Only for the members at the coefficients $\Delta\widetilde{\mathcal{R}}^{(k,k',x)}_{PT(\mathrm{VV})}(n\ell j\ n'\ell' j'\ n'\ell' j')$, $\Delta\widetilde{\mathcal{R}}^{(k,k',x)}_{PT(\mathrm{VV})}(n\ell j\ n'\ell' j'\ n''\ell'' j'')$, $\Delta\widetilde{\widetilde{\mathcal{R}}}^{(k,k',x)}_{PT(\mathrm{CV})}(n\ell j\ n'\ell' j'\ n'\ell' j')$, and $\Delta\widetilde{\widetilde{\mathcal{R}}}^{(k,k',x)}_{PT(\mathrm{CV})}(n\ell j\ n'\ell' j'\ n''\ell'' j'')$ such an extension of the library `librang` [20] is needed in order to find the following reduced matrix elements (see (31) or (24) in [16] and (23) in [17]):

$$\left\langle \Psi \left\| \left[\left[\tilde{a}^{(j)} \times a^{(j)}\right]^{(k)} \times \left[\left[a^{(j')} \times \tilde{a}^{(j')}\right]^{(x)} \times \left[a^{(j')} \times \tilde{a}^{(j')}\right]^{(k')} \right]^{(k)} \right]^{(0)} \right\| \Psi \right\rangle, \tag{32}$$

$$\left\langle \Psi \left\| \left[\left[\left[\tilde{a}^{(j)} \times a^{(j)}\right]^{(k)} \times \left[a^{(j'')} \times \tilde{a}^{(j'')}\right]^{(x)} \right]^{(k')} \times \left[a^{(j')} \times \tilde{a}^{(j')}\right]^{(k')} \right]^{(0)} \right\| \Psi \right\rangle, \tag{33}$$

$$\left\langle \Psi \left\| \left[\left[a^{(j)} \times \tilde{a}^{(j)}\right]^{(k)} \times \left[\left[a^{(j')} \times \tilde{a}^{(j')}\right]^{(x)} \times \left[\tilde{a}^{(j')} \times a^{(j')}\right]^{(k')} \right]^{(k)} \right]^{(0)} \right\| \Psi \right\rangle, \tag{34}$$

$$\left\langle \Psi \left\| \left[\left[\left[a^{(j)} \times \tilde{a}^{(j)}\right]^{(k)} \times \left[\tilde{a}^{(j'')} \times a^{(j'')}\right]^{(x)} \right]^{(k')} \times \left[\tilde{a}^{(j')} \times a^{(j')}\right]^{(k')} \right]^{(0)} \right\| \Psi \right\rangle. \tag{35}$$

Below we discuss how to calculate these reduced matrix elements (32)–(35), i.e., to calculate spin-angular coefficients of three-particle Feynman diagrams VV_3 and CV_7 from Figure 1 for accounting for (21), (22), (4) and (5) correlations by extending and using the library `librang` [20], in a way that makes the calculations as efficient as possible, i.e., based on the combination of the angular momentum theory as described in Jucys and Bandzaitis [33], the concept of irreducible tensorial sets (Judd [36], Rudzikas and Kaniauskas [37]), the generalized graphical approach (Gaigalas et al. [34]), the second quantization in coupled tensorial form (Rudzikas and Kaniauskas [37]), the quasispin approach (Rudzikas [38]), and the use of reduced coefficients of fractional parentage (Gaigalas et al. [39,40]) as was done in papers by Gaigalas et al. [20,21]. For additional information about the calculation of these reduced matrix elements, see Appendix A.

4.1. The Third Type of Valence–Valence and Core–Valence Correlations

For these types of correlations, the calculation of the spin-angular coefficients at the members of $\Delta\widetilde{\mathcal{R}}^{(J_1,J_2,x)}_{PT(\mathrm{VV})}(n\ell j\ n'\ell' j'\ n'\ell' j')$ (see (24) or (26) in [16]) and $\Delta\widetilde{\widetilde{\mathcal{R}}}^{(J_1,J_2,x)}_{PT(\mathrm{CV})}(n\ell j\ n'\ell' j'\ n'\ell' j')$ (see (21) or (23) in [17]) is more complex and is not fully supported by the library `librang` [20]. It is essential that these problematic terms have the following tensorial product (see (6) in [16]) from (32)

$$\left[\left[\tilde{a}^{(j_m)} \times a^{(j_m)}\right]^{(J_1)} \times \left[\left[a^{(j_n)} \times \tilde{a}^{(j_n)}\right]^{(x)} \times \left[a^{(j_n)} \times \tilde{a}^{(j_n)}\right]^{(J_2)}\right]^{(J_1)}\right]^{(0)} \tag{36}$$

and the following (see (6) in [17]) from (34)

$$\left[\left[a^{(j_m)}\times\tilde{a}^{(j_m)}\right]^{(J_1)}\times\left[\left[a^{(j_n)}\times\tilde{a}^{(j_n)}\right]^{(x)}\times\left[\tilde{a}^{(j_n)}\times a^{(j_n)}\right]^{(J_2)}\right]^{(J_1)}\right]^{(0)}. \quad (37)$$

We now discuss below how this problem can be addressed.

A peculiarity of the methodology [21,22,41] is that in the expression (24) in [20] for the calculation of the reduced matrix element of the two-particle operator

$$\left\langle\gamma_\alpha J\middle\|\,\widehat{G}^{(k_j\ k_j\ 0)}\left(n_i\ell_ij_i,n_j\ell_jj_j,n_{i'}\ell_{i'}j_{i'},n_{j'}\ell_{j'}j_{j'}\right)\middle\|\gamma_\beta J'\right\rangle$$
$$=\sum_{\kappa_{12}}(-1)^{\Delta}\,\Theta'\left(n_i\ell_ij_i,n_j\ell_jj_j,n_{i'}\ell_{i'}j_{i'},n_{j'}\ell_{j'}j_{j'},\ \Xi\right)\ T\left(j_i,j_j,j_{i'},j_{j'},\Lambda^{bra},\Lambda^{ket},\Xi,\Gamma\right)$$
$$\times\ R\left(j_i,j_j,j_{i'},j_{j'},\Lambda^{bra},\Lambda^{ket},\Gamma\right), \quad (38)$$

the recoupling matrix $R\left(j_i,j_j,j_{i'},j_{j'},\Lambda^{bra},\Lambda^{ket},\Gamma\right)$, the submatrix element $T\left(j_i,j_j,j_{i'},j_{j'},\Lambda^{bra},\Lambda^{ket},\Xi,\Gamma\right)$, the phase factor Δ, and $\Theta'\left(n_i\ell_ij_i,n_j\ell_jj_j,n_{i'}\ell_{i'}j_{i'},n_{j'}\ell_{j'}j_{j'},\ \Xi\right)$, which is proportional to the radial part, are easily separated from each other and can be treated differently. This makes the methodology flexible and allows it to be easily extended to include new class/type operators, such as the three-particle operators (36) and (37) we are considering. The paper [21] describes how the expression (11) in [21] is implemented in the library in a regular way. By the way, the rank k_j for operator $\widehat{G}^{(k_j\ k_j\ 0)}$ in Equation (38) is equal to J_1 for the third type of VV and CV correlations.

In the following, we will discuss only those aspects of the calculation matrix element of three-particle Feynman diagrams A_5 from [16,17] with the tensorial products (36) and (37), which were not covered in the paper [20]. The phase factor Δ and $\Theta'\left(n_i\ell_ij_i,n_j\ell_jj_j,n_{i'}\ell_{i'}j_{i'},n_{j'}\ell_{j'}j_{j'},\ \Xi\right)$ do not bring any additional problems to the calculation of the spin-angular part of this case, i.e., Δ, according to the methodology [21], is zero, and the $\Theta'\left(n_i\ell_ij_i,n_j\ell_jj_j,n_{i'}\ell_{i'}j_{i'},n_{j'}\ell_{j'}j_{j'},\ \Xi\right)$, which is proportional to the radial part, is found in a regular way as it was found in papers [12–15]. For the third type of VV correlations, $\Theta'\left(n_i\ell_ij_i,n_j\ell_jj_j,n_{i'}\ell_{i'}j_{i'},n_{j'}\ell_{j'}j_{j'},\ \Xi\right)$ is as follows (see Table 2 in [16])

$$\Theta'\left(n_i\ell_ij_i,n_j\ell_jj_j,n_{i'}\ell_{i'}j_{i'},n_{j'}\ell_{j'}j_{j'},\ \Xi\right)=2\sum_r(-1)^{-j_m+j_n+x}\sqrt{[J_1,J_2,x]}\ \mathcal{G}(J_1\ J_2\ x,\ nn,\ mr) \quad (39)$$

and for the third type of CV correlations it is as follows(see Table 2 in [17])

$$\Theta'\left(n_i\ell_ij_i,n_j\ell_jj_j,n_{i'}\ell_{i'}j_{i'},n_{j'}\ell_{j'}j_{j'},\ \Xi\right)=2\sum_a(-1)^{j_m+j_n}\sqrt{[J_1,J_2,x]}\ \mathcal{G}'(J_1\ J_2\ x,\ nn,\ ma), \quad (40)$$

where in both cases (39) and (40) $n_i\ell_ij_i\equiv n$, $n_j\ell_jj_j\equiv m$, $n'_i\ell'_ij'_i\equiv n$, $n'_j\ell'_jj'_j\equiv m$, and $\Xi\equiv J_1\ J_2\ x$.

Although expressions (39) and (40) appear very similar visually, they contain different coefficients $\mathcal{G}(J_1\ J_2\ x,\ nn,\ mr)$ and $\mathcal{G}'(J_1\ J_2\ x,\ nn,\ ma)$ and different phases. This is related to the fact that the Feynman diagram expressions themselves differ in phase, multipliers, and tensorial structure. For example, in the expression for the VV_3 diagram, we have the phase factor $(-1)^{k+k'}$, whereas in the case of the CV_7 diagram, we have the factor (-1). Meanwhile, the tensorial structure in the first case is

$$\left[\left[\left[\ a^{(j_n)}\times\tilde{a}^{(j_m)}\ \right]^{(k)}\times\left[\ a^{(j_n)}\times\tilde{a}^{(j_n)}\ \right]^{(x)}\right]^{(k')}\times\left[\ a^{(j_m)}\times\tilde{a}^{(j_n)}\ \right]^{(k')}\right]^{(0)}, \quad (41)$$

and in the second case is:

$$\left[\left[\left[\, a^{(j_m)} \times \tilde{a}^{(j_n)} \,\right]^{(k)} \times \left[\, \tilde{a}^{(j_n)} \times a^{(j_n)} \,\right]^{(x)}\right]^{(k')} \times \left[\, a^{(j_n)} \times \tilde{a}^{(j_m)} \,\right]^{(k')}\right]^{(0)}. \tag{42}$$

These expressions are not suitable for calculating the reduced matrix elements of the above operators because they do not fully exploit the advantages of the Racah algebra. Thus, they must be rearranged accordingly. For the tensorial product (41), using Expression (8) from the paper [16], and for the tensorial product (42), using Expression (11) from the paper [17], we obtain new expressions for which the [21,22] method can already be used when calculating reduced matrix elements. Expressions (39) and (40) represent the terms of the triple tensorial product. For almost all of the multipliers and intermediate sums in these terms, the corresponding notations $\mathcal{G}(J_1\, J_2\, x,\, nn,\, mr)$ and $\mathcal{G}'(J_1\, J_2\, x,\, nn,\, ma)$ have been introduced. Additionally, the term $\dfrac{-1}{D}$ and the phase $(-1)^{k'}$ are included in the multipliers $\mathcal{G}(J_1\, J_2\, x,\, nn,\, mr)$ and $\mathcal{G}'(J_1\, J_2\, x,\, nn,\, ma)$. After summing all the phase factors defined in the Feynman diagram expression and the phase factors resulting from the tensorial structure transformations listed above, and including the definitions of the $\mathcal{G}(J_1\, J_2\, x,\, nn,\, mr)$ and $\mathcal{G}'(J_1\, J_2\, x,\, nn,\, ma)$ factors, we obtain the following phases, i.e., in Expression (39), they are:

$$k + k' + j_m + j_n + k + x - 1 - k' = j_m + j_n + x - 1 = -j_m + j_n + x,$$

and in Expression (40), it is:

$$1 + j_m + j_n + k' - 1 - k' = j_m + j_n.$$

As we can see, although at first glance the structure of Expressions (39) and (40) is very similar, their derivation is quite different, and they differ not only in the phase but also in the values of the multipliers $\mathcal{G}(J_1\, J_2\, x,\, nn,\, mr)$ and $\mathcal{G}'(J_1\, J_2\, x,\, nn,\, ma)$.

So it remains to discuss finding the values of the recoupling matrix $R\left(j_i, j_j, j_{i'}, j_{j'}, \Lambda^{bra}, \Lambda^{ket}, \Gamma\right)$ and the submatrix element $T\left(j_i, j_j, j_{i'}, j_{j'}, \Lambda^{bra}, \Lambda^{ket}, \Xi, \Gamma\right)$, which are related to the calculation of reduced matrix elements of operators (36) and (37). Figure 9 shows how and which subroutines from the program library `librang` should be used and which expressions should be added for their calculation of them.

Since we can schematically rewrite the tensorial products (36) and (37) as the tensorial product of two operators $A^{(J_1)}(n_m j_m)$ and $B^{(J_1)}(n_n j_n)$ acting on different subshells

$$\left[\, A^{(J_1)}(n_m j_m) \times B^{(J_1)}(n_n j_n) \,\right]^{(0)}, \tag{43}$$

the algebraic expression of the recoupling matrix $R\left(j_i, j_j, j_{i'}, j_{j'}, \Lambda^{bra}, \Lambda^{ket}, \Gamma\right)$ can be used from the paper (see (19) in [21]); i.e., first of all, the selection rules (see Table 3 in [20]) for the recoupling matrix can be checked by the subroutine `RECO` (see Section 3.2.3 in [20]), and after that, it can be computed by the subroutine `RECO2` (see Section 3.2.4 in [20] and Figure 9). Therefore, the library's `librang` existing capabilities are entirely sufficient for calculating $R\left(j_i, j_j, j_{i'}, j_{j'}, \Lambda^{bra}, \Lambda^{ket}, \Gamma\right)$.

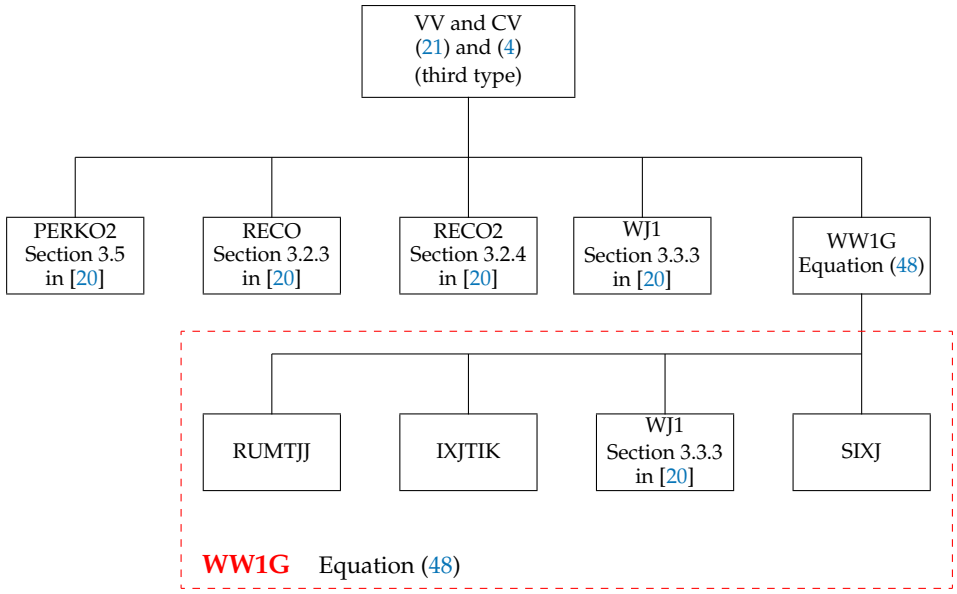

Figure 9. The scheme for the calculation of reduced matrix elements of operators (36) and (37), i.e., the scheme for the spin-angular coefficients calculation of Feynman diagrams VV_3 from [16] and CV_7 from [17] for correlations (21) and (4).

As far as the submatrix element $T\left(j_i, j_j, j_{i'}, j_{j'}, \Lambda^{bra}, \Lambda^{ket}, \Xi, \Gamma\right)$ is concerned, the situation is different. The $T\left(j_i, j_j, j_{i'}, j_{j'}, \Lambda^{bra}, \Lambda^{ket}, \Xi, \Gamma\right)$ is equal to the matrix element of the tensorial product (43) between bra and ket functions containing only those subsells to which this tensor operator acts, i.e.,

$$\begin{aligned} & T\left(j_i, j_j, j_{i'}, j_{j'}, \Lambda^{bra}, \Lambda^{ket}, \Xi, \Gamma\right) \\ & \quad = \left\langle (n_m \ell_m)\, j_m^{w_m}\, \alpha_m Q_m J_m \;\; (n_n \ell_n)\, j_n^{w_n}\, \alpha_n Q_n J_n \right. \\ & \qquad \left\| A^{(J_1)}(n_m j_m)\, B^{(J_1)}(n_n j_n) \right\| \\ & \qquad \left. (n_n \ell_m)\, j_m^{w'_m}\, \alpha'_m Q'_m J'_m \;\; (n_n \ell_n)\, j_n^{w'_n}\, \alpha'_n Q'_n J'_n \right\rangle, \end{aligned} \tag{44}$$

where the binding of the ranks J_1, J_1, to 0 of the tensorial structure (43) is already included in the recoupling matrix $R\left(j_i, j_j, j_{i'}, j_{j'}, \Lambda^{bra}, \Lambda^{ket}, \Gamma\right)$, $n_i \ell_i j_i \equiv n$, $n_j \ell_j j_j \equiv m$, $n'_i \ell'_i j'_i \equiv n$, $n'_j \ell'_j j'_j \equiv m$, $\Xi \equiv J_1\, J_2\, x$, $\Lambda^{bra} \equiv Q_m J_m Q_n J_n$, $\Lambda^{ket} \equiv Q'_m J'_m Q'_n J'_n$, and Γ is an empty array. In this case, the tensorial product can be simply split into two parts, i.e.,

$$A^{(J_1)}(n_m j_m) \;\equiv \left[a_{m_{q1}}^{(q\, j_m)} \times a_{m_{q2}}^{(q\, j_m)}\right]^{(J_1)} \tag{45}$$

and

$$B^{(J_1)}(n_n j_n) \;\equiv \left[\left[a_{m_{q3}}^{(q\, j_n)} \times a_{m_{q4}}^{(q\, j_n)}\right]^{(x)} \times \left[a_{m_{q5}}^{(q\, j_n)} \times a_{m_{q6}}^{(q\, j_n)}\right]^{(J_2)}\right]^{(J_1)}. \tag{46}$$

Here, we use the quasispin formalism [38,40,41], where the operators of second quantization are the components of an irreducible tensor of rank $q = 1/2$ in a quasispin space [42].

$$a_{m_q\, m_j}^{(q\; j)} = \begin{cases} a_{m_j}^{(j)} & \text{for } m_q = +\frac{1}{2}, \\ \tilde{a}_{m_j}^{(j)} & \text{for } m_q = -\frac{1}{2}. \end{cases} \tag{47}$$

In the case where $m_{q2} = m_{q3} = m_{q5} = \frac{1}{2}$ and $m_{q1} = m_{q4} = m_{q6} = -\frac{1}{2}$, then the tensorial product (43) corresponds to the tensorial product (36) and where $m_{q1} = m_{q3} = m_{q6} = \frac{1}{2}$ and $m_{q2} = m_{q4} = m_{q5} = -\frac{1}{2}$, then the tensorial product (43) corresponds to the tensorial product (37).

Since the tensorial product can be split into two parts (45) and (46), the reduced matrix elements of these two members $A^{(J_1)}(n_m j_m)$ and $B^{(J_1)}(n_n j_n)$ should be considered separately (because they act on different subshells, and the binding of the ranks of the tensorial structure, as was mentioned above, is already included in the recoupling matrix). Subroutine `WJ1` (see Section 3.3.3 in [20] and Figure 9) finds the reduced matrix element of operator (45), while the library `librang` has no suitable subroutine for computing the reduced matrix element of the operator (46). To find the latter, it is required to use an expression such as

$$\begin{aligned}\left\langle (n_n\ell_n)\, j_n^w\, \alpha QJ \middle\| \left[\left[a^{(q\,j_n)}_{m_{q3}} \times a^{(q\,j_n)}_{m_{q4}}\right]^{(x)} \times \left[a^{(q\,j_n)}_{m_{q5}} \times a^{(q\,j_n)}_{m_{q6}}\right]^{(J_2)}\right]^{(J_1)} \middle\| (n_n\ell_n)\, j_n^{w'}\, \alpha' Q' J' \right\rangle \\ = (-1)^{J+J'+J_1} \sqrt{[J_1]} \sum_{\alpha'' Q'' J''} \begin{Bmatrix} x & J_2 & J_1 \\ J' & J & J'' \end{Bmatrix} \\ \times \left\langle (n_n\ell_n)\, j_n^w\, \alpha QJ \middle\| \left[a^{(q\,j_n)}_{m_{q3}} \times a^{(q\,j_n)}_{m_{q4}}\right]^{(x)} \middle\| (n_n\ell_n)\, j_n^{w''}\, \alpha'' Q'' J'' \right\rangle \\ \times \left\langle (n_n\ell_n)\, j_n^{w''}\, \alpha'' Q'' J'' \middle\| \left[a^{(q\,j_n)}_{m_{q5}} \times a^{(q\,j_n)}_{m_{q6}}\right]^{(J_2)} \middle\| (n_n\ell_n)\, j_n^{w'}\, \alpha' Q' J' \right\rangle. \end{aligned} \quad (48)$$

Therefore, the library `librang` has been extended by subroutine `WW1G` (see Figure 9), which determines the value of the reduced matrix elements of the operator (46) according to Expression (48). The red-framed WW1G in Figure 9 shows the structure of this new routine, `WW1G`. There subroutine `IXJTIK` checks the triangular delta functions of the 6*j*-coefficients from Equation (48), subroutine `SIXJ` calculates the values of this coefficient if the triangular delta functions are not zero, and subroutine `WJ1` (see Section 3.3.3 in [20]) calculates the reduced matrix elements of the pairs $\left[a^{(q\,j)}_{m_q} \times a^{(q\,j)}_{m_{q'}}\right]^{(k)}$ of operators of the second quantization from (48). In this case, the subroutine `WJ1` is called twice. Meanwhile, subroutine `RUMTJJ` prepares the corresponding input arrays for these calculations. Meanwhile, the subroutine `PERKO2` outside the red frame WW1G in Figure 9 is the interface between GRASP2018 [6] and the SQ routines group (see Section 3.3 in [20]) from the library `librang`. For additional information about the subroutine, see Appendix B.

All of the above implementations allow simple/easy calculation of the third type of VV and CV correlations with minimal program library `librang` expansion.

4.2. The Fourth Type of Valence–Valence and Core–Valence Correlations

For these types of correlations, the calculation of the spin-angular coefficients at the members of $\Delta\widetilde{\mathcal{R}}^{(J_1,J_2,x)}_{PT(\mathrm{VV})}(n\ell j\; n'\ell' j'\; n''\ell'' j'')$ (see (24) or (26) in [16]) and $\Delta\widetilde{\widetilde{\mathcal{R}}}^{(J_1,J_2,x)}_{PT(\mathrm{CV})}(n\ell j\; n'\ell' j'\; n''\ell'' j'')$ (see (21) or (23) in [17]) is complex, and we need to discuss how to find them. These problematic terms have the following tensorial products (see (14) and (21) in [16]) from (33)

$$\left[\left[\left[\tilde{a}^{(j_m)} \times a^{(j_m)}\right]^{(J_1)} \times \left[a^{(j_p)} \times \tilde{a}^{(j_p)}\right]^{(x)}\right]^{(J_2)} \times \left[a^{(j_n)} \times \tilde{a}^{(j_n)}\right]^{(J_2)}\right]^{(0)} \quad (49)$$

and the following (see (14) and (18) in [17]) from (35)

$$\left[\left[\left[a^{(j_m)} \times \tilde{a}^{(j_m)}\right]^{(J_1)} \times \left[\tilde{a}^{(j_p)} \times a^{(j_p)}\right]^{(x)}\right]^{(J_2)} \times \left[\tilde{a}^{(j_n)} \times a^{(j_n)}\right]^{(J_2)}\right]^{(0)}. \quad (50)$$

Since we can schematically rewrite the tensorial products (49) and (50) as the tensorial product of three operators, $A^{(J_1)}(n_m j_m)$, $B^{(x)}(n_p j_p)$, $C^{(J_2)}(n_n j_n)$ acting on different subshells

$$\left[\left[A^{(J_1)}(n_m j_m) \times B^{(x)}(n_p j_p)\right]^{(J_2)} \times C^{(J_2)}(n_n j_n)\right]^{(0)}, \tag{51}$$

the algebraic expression of the recoupling matrix $R\left(j_i, j_j, j_{i'}, j_{j'}, \Lambda^{bra}, \Lambda^{ket}, \Gamma\right)$ (see Equation (38)) can be used from the paper (see (19) in [21]), i.e., first of all, the selection rules for the recoupling matrix can be checked by the subroutine `RECO` (see Section 3.2.3 in [20]), and after that, it can be computed by the subroutine `RECO2` (see Section 3.2.4 in [20]) in case $J_1 = 0$ or by the subroutine `REC3` (see Section 3.2.5 in [20]) in case $J_1 \neq 0$ (see Figure 10). Therefore, the library's `librang` existing capabilities are entirely sufficient for calculating $R\left(j_i, j_j, j_{i'}, j_{j'}, \Lambda^{bra}, \Lambda^{ket}, \Gamma\right)$.

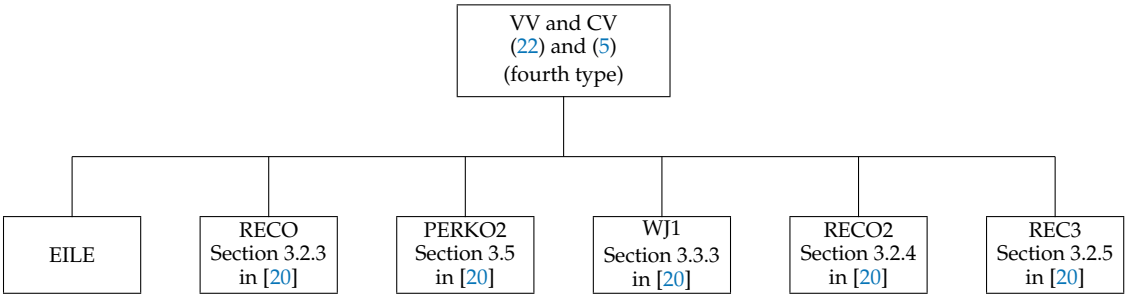

Figure 10. The scheme for the calculation of reduced matrix elements of operators (49) and (50), i.e., the scheme for the spin-angular coefficients calculation of Feynman diagrams A_5 and A_6 from [16,17] for correlations (22) and (5).

The submatrix element $T\left(j_i, j_j, j_{i'}, j_{j'}, \Lambda^{bra}, \Lambda^{ket}, \Xi, \Gamma\right)$ (see Equation (38)) has the following form for the fourth type of VV and CV correlations

$$\begin{aligned} &T\left(j_i, j_j, j_{i'}, j_{j'}, \Lambda^{bra}, \Lambda^{ket}, \Xi, \Gamma\right) \\ &\quad = \Big\langle (n_m \ell_m)\, j_m^{w_m}\, \alpha_m Q_m J_m \; (n_n \ell_n)\, j_n^{w_n}\, \alpha_n Q_n J_n \; j_p^{w_p}\, \alpha_p Q_p J_p \\ &\qquad\qquad \Big\| A^{(J_1)}(n_m j_m)\, B^{(x)}(n_p j_p)\, C^{(J_2)}(n_n j_n) \Big\| \\ &\qquad\qquad (n_n \ell_m)\, j_m^{w'_m}\, \alpha'_m Q'_m J'_m \; (n_n \ell_n)\, j_n^{w'_n}\, \alpha'_n Q'_n J'_n \; j_p^{w'_p}\, \alpha'_p Q'_p J'_p \Big\rangle. \end{aligned} \tag{52}$$

In this case, the tensorial product can be split into three parts, i.e.,

$$A^{(J_1)}(n_m j_m) \equiv \left[a_{m_{q1}}^{(q\, j_m)} \times a_{m_{q2}}^{(q\, j_m)}\right]^{(J_1)}, \tag{53}$$

$$B^{(x)}(n_p j_p) \equiv \left[a_{m_{q3}}^{(q\, j_p)} \times a_{m_{q4}}^{(q\, j_p)}\right]^{(x)}, \tag{54}$$

and

$$C^{(J_2)}(n_n j_n) \equiv \left[a_{m_{q5}}^{(q\, j_n)} \times a_{m_{q6}}^{(q\, j_n)}\right]^{(J_2)}. \tag{55}$$

In the case where $m_{q2} = m_{q3} = m_{q5} = \frac{1}{2}$ and $m_{q1} = m_{q4} = m_{q6} = -\frac{1}{2}$, then the tensorial product (51) corresponds to the tensorial product (49), and when $m_{q1} = m_{q4} = m_{q6} = \frac{1}{2}$ and $m_{q2} = m_{q3} = m_{q5} = -\frac{1}{2}$, then the tensorial product (51) corresponds to the tensorial product (50).

These three members $A^{(J_1)}(n_m j_m)$, $B^{(x)}(n_p j_p)$, and $C^{(J_2)}(n_n j_n)$ in (51) should be considered separately (because they act on different subshells, and the binding of the ranks J_1, x, to J_2 and J_2, J_2, to 0 of the tensorial structure (51) is already included in the recoupling matrix). Subroutine `WJ1` (see Section 3.2.3 in [20] and Figure 10) finds the reduced matrix element of all these operators (53)–(55). In this case, this subroutine is called three times. The subroutine `EILE` reorders the operators of second quantization (49) and (50) in the same order as the subshells in the CSF from the matrix-reduced element. The rest of the subroutines are the same as in Figure 9.

So in this case, no new subroutines have to be created. The old ones are enough, but to do these calculations, it is necessary to choose the right subroutines already existing in the library and to call them in the right order with the right argument values, as schematically shown in Figure 10.

Finally, as regards the members Δ and $\Theta'\left(n_i\ell_i j_i, n_j\ell_j j_j, n_{i'}\ell_{i'} j_{i'}, n_{j'}\ell_{j'} j_{j'}, \Xi\right)$ in Formula (38), they do not pose any problem, as it was in Section 4.1. The Δ, according to the methodology [21], is equal to zero. Meanwhile, the expressions for member $\Theta'\left(n_i\ell_i j_i, n_j\ell_j j_j, n_{i'}\ell_{i'} j_{i'}, n_{j'}\ell_{j'} j_{j'}, \Xi\right)$ are published in papers (see Table 3 in [16] and Table 3 in [17]) and are, respectively, as follows for the fourth type of VV correlation

$$\begin{aligned}
&\Theta'\left(n_i\ell_i j_i, n_j\ell_j j_j, n_{i'}\ell_{i'} j_{i'}, n_{j'}\ell_{j'} j_{j'}, \Xi\right)\\
&= (-1)^{j_m+j_n}\sqrt{[J_1, J_2, x]}\sum_r\left\{(-1)^{x+1}\mathcal{G}(J_1\,J_2\,x,\, np,\, mr)\right.\\
&\left.+\sum_{k_1,k_2,k_3}(-1)^{J_1+J_2+k_1}\,[k_3]\begin{Bmatrix} j_n & j_p & k_3\\ k_1 & k_2 & j_r\end{Bmatrix}\mathcal{Q}(k_1k_2, np, mr)\,\mathcal{C}_{12j}(j_m j_n j_p,\, k_1\,k_2\,k_3,\, J_1\,J_2\,x)\right\}\\
&\times\left(1+\mathrm{P}\begin{pmatrix} n & \rightleftharpoons & p\\ k_1 & \rightleftharpoons & k_2\\ J_2 & \rightleftharpoons & x\end{pmatrix}\right)
\end{aligned}\tag{56}$$

and for the fourth type of CV correlation

$$\begin{aligned}
&\Theta'\left(n_i\ell_i j_i, n_j\ell_j j_j, n_{i'}\ell_{i'} j_{i'}, n_{j'}\ell_{j'} j_{j'}, \Xi\right)\\
&= -(-1)^{j_m+j_n}\sqrt{[J_1, J_2, x]}\sum_a\left\{(-1)^{x+1}\mathcal{G}'(J_1\,J_2\,x,\, ma,\, np)\right.\\
&\left.+\sum_{k_1,k_2,k_3}(-1)^{J_1+J_2+k_1}\,[k_3]\begin{Bmatrix} j_n & j_p & k_3\\ k_1 & k_2 & j_a\end{Bmatrix}\mathcal{Q}(k_1k_2, ma, np)\,\mathcal{C}_{12j}(j_m j_n j_p,\, k_1\,k_2\,k_3,\, J_1\,J_2\,x)\right\}\\
&\times\left(1+\mathrm{P}\begin{pmatrix} n & \rightleftharpoons & p\\ k_1 & \rightleftharpoons & k_2\\ J_2 & \rightleftharpoons & x\end{pmatrix}\right).
\end{aligned}\tag{57}$$

In the expressions, (1 + P) represents two members, where the second member is obtained from the first by making replacements marked in P. This simultaneously simplifies the expression and reveals the symmetry between the two members. Moreover, the $\Theta'\left(n_i\ell_i j_i, n_j\ell_j j_j, n_{i'}\ell_{i'} j_{i'}, n_{j'}\ell_{j'} j_{j'}, \Xi\right)$ member does not belong to the spin-angular part but to the amplitude of the effective operator. It is therefore only needed to find the reduced matrix element of the Feynman diagram according to Formula (38).

5. Calculation of Core–Valence, Core, Core–Core, and Valence–Valence with a New Approach

This section presents computations using the method based on the Rayleigh–Schrödinger perturbation theory in an irreducible tensorial form [12–17]. The developed RSMBPT method was applied to select the most significant configuration state functions and further used them for solving the self-consistent field equations. The radial wavefunctions obtained by the RSMBPT method were used for further RCI investigations in which the RSMBPT method was also applied to determine the most important correlations of various types.

The main goal is to demonstrate how the developed method can be used at different stages of the calculation process (MCDHF and RCI). It is important to check how it works, how the results are reproduced, and how they agree compared with regular GRASP calculations. This is a newly developed method, and this is only the first paper demonstrating the estimation of complete (CV, C, CC, and VV) correlations using RSMBPT. Light atoms/ions are the best candidates for such investigations and standard practice for presentations of new methods. Therefore, Ar II, which has a relatively large core, was selected as the test case for such investigations.

For this purpose, 3 energy levels ($3s^2 3p^5\ ^2P^o_{1/2,3/2}$ and $3s3p^6\ ^2S_{1/2}$) and electric dipole (E1) transitions between these states were computed for Ar II. Since the $3s^2 3p^5\ ^2P^o_{1/2,3/2}$ states are pure, and the $3s3p^6\ ^2S_{1/2}$ state has strong mixing with the $3s^2 3p^4 3d$ configuration, this configuration was included in the MR set. In the present paper, the MCDHF computations were performed simultaneously for even and odd states using the extended optimal level (EOL) scheme [2]. As a first step, MCDHF calculations were performed for the radial wave functions of orbitals belonging to the MR set; these were used in further computations. In the next steps, MCDHF and RCI calculations were performed using the RSMBPT method [12–17]. The subsequent subsections provide a detailed description of these calculations, while the results are presented in Section 5.2. It is important to note that that both (MCDHF and RCI) calculations were performed, including only CSFs that have a non-zero spin-angular part of matrix elements with at least one CSF in the MR. The Breit interactions and leading QED effects (the vacuum polarization and self-energy corrections) were taken into account at the RCI stage.

5.1. Computational Scheme Using the RSMBPT Method

5.1.1. The CSF Basis Selection Procedure Applying the RSMBPT Method

Using the RSMBPT method, the orbital space is divided into three sets: F, F', and G (see Ref. [12] for details). The F set defines the core, F'-valence, and G-virtual subshells (these belong to orbital sets (OS)). The classification of subshells in the present calculations is presented in Table 1.

Table 1. The classification of the orbital space applying the RSMBPT method.

Set	Subshells
F	1s, 2s, 2p$_-$, 2p
F'	3s, 3p$_-$, 3p, 3d$_-$, 3d
G	OS_1 = {4s,4p$_-$,4p,4d$_-$,4d,4f$_-$,4f} OS_2 = {5s,5p$_-$,5p,5d$_-$,5d,5f$_-$,5f,5g$_-$,5g} OS_3 = {6s,6p$_-$,6p,6d$_-$,6d,6f$_-$,6f,6g$_-$,6g,6h$_-$,6h} OS_4 = {7s,7p$_-$,7p,7d$_-$,7d,7f$_-$,7f,7g$_-$,7g,7h$_-$,7h} OS_5 = {8s,8p$_-$,8p,8d$_-$,8d,8f$_-$,8f,8g$_-$,8g,8h$_-$,8h}

The estimation of the chosen correlation type applying the RSMBPT method is analogous to the procedure used in previous studies [12–17]. The contribution of each K'

configuration is computed according to Equation (31). Further, these configurations are arranged in descending order based on the computed impact of the correlations and are selected by the correlations' impact with the specified fraction of the total correlations' contribution. Only K' configurations with a correlation contribution larger than 1.0×10^{-11} are included in the computations; the remaining configurations are neglected. It is important to note that the assessment of the correlations using the stationary second-order Rayleigh–Schrödinger many-body perturbation theory in an irreducible tensorial form is done for the Coulomb interaction. Since the V (Equation (26)) and C (Equation (27)) correlations can not be included using the RSMBPT method, they were incorporated into the calculations in a regular way.

5.1.2. MCDHF Computations Applying the RSMBPT Method

The radial wavefunctions were computed, including different types of correlations. There were four types of MCDHF computations performed: (i) including only VV correlations; (ii) including VV and C correlations; (iii) including VV, C, and CV correlations; (iv) including VV, C, CV, and CC correlations. The procedure for applying the RSMBPT method to construct the CSF basis and then using it to solve the self-consistent field equations is described in [16]. In this work, the procedure is repeated, focusing on the main steps. Figure 11 shows the typical sequence of calculation steps for solving the self-consistent field equations using the RSMBPT method. Firstly, the CSF basis of the OS_1 is generated in the regular way (step 1 in Figure 11). The next step in any MCDHF calculation with a chosen type of correlation is to estimate the initial radial wavefunctions of the OS_1 using the Thomas–Fermi potential (step 2 in Figure 11). Next, the contributions of correlations are estimated applying the RSMBPT method, and the CSF basis is constructed by selecting the most significant correlations with a specified fraction of 99.95% (steps 3 and 4 in Figure 11). Then, the self-consistent field equations are solved using a constructed CSF basis (step 5 in Figure 11). In step 6, the convergence of the SELF-CONSISTENCY and NORM-1 parameters is studied and estimated. Once convergence has been achieved, the calculations finish and the radial wavefunctions of the next *OS* can be computed. Otherwise, the obtained radial wavefunctions are used as the initial ones. The selection procedure of the most significant correlations, applying the RSMBPT method with revised radial wavefunctions, and MCDHF computation is repeated until convergence is achieved (steps 3–5 are repeated).

Further, the radial wavefunctions of the new *OS* are computed. The same sequence of calculation steps is applied when the radial wavefunctions of the OS_2 and further new *OS*–OS_3, OS_4, and OS_5 are computed. It is important to highlight a few points described below. Computing radial wavefunctions of the OS_2, the initial radial wavefunctions of the OS_1 and OS_2 are used in the Thomas–Fermi potential approximation. Then the contributions of correlations from both (OS_1 and OS_2) sets are estimated, applying the RSMBPT method, and the most significant correlations are selected. This is performed in order to ensure that the contributions of correlations from both (OS_1 and OS_2) sets are estimated with the same level of accuracy as radial wavefunctions. The constructed CSF basis is used for solving the self-consistent field equations of OS_2. In this step, the OS_1 radial wave functions are taken from the final OS_1 computations and are fixed. The obtained radial wavefunctions are taken as initial, and the selection procedure of CSFs is repeated, along with a solution of the self-consistent field equations, until convergence is achieved (as was done in the case of OS_1). Results from MCDHF computations, including chosen correlations according to the RSMBPT method, are marked as VV MCDHF (RSMBPT) (when only VV correlations are included), VV + C MCDHF (RSMBPT) (when VV and C correlations are included), VV + C + CV MCDHF (RSMBPT) (when VV, C, and CV

correlations are included), and VV + C + CV + CC MCDHF (RSMBPT) (when VV, C, CV, and CC correlations are included).

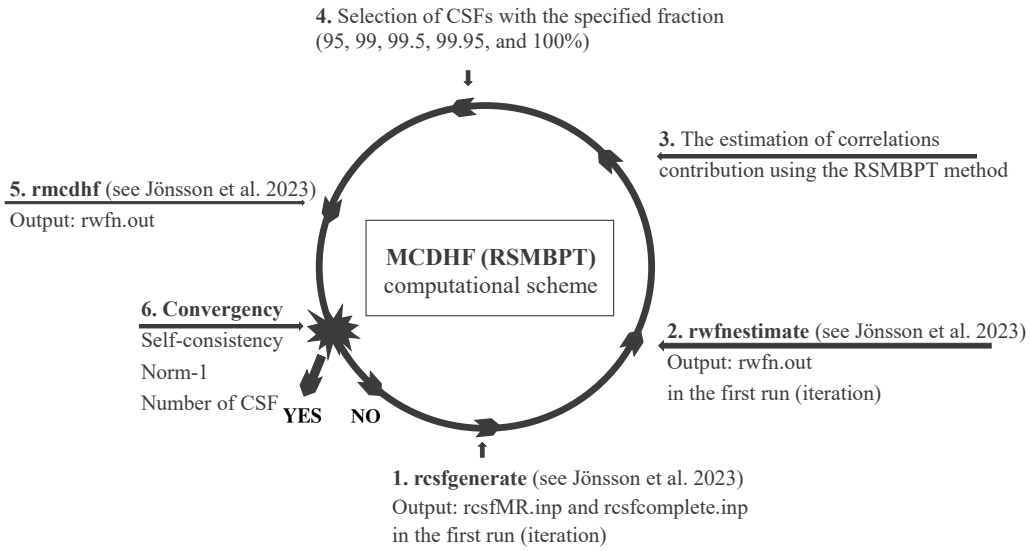

Figure 11. Typical sequence of calculation steps for solving the self-consistent field equations using the RSMBPT method. Jönsson et al. 2023 in the figure marks Ref. [9].

5.1.3. RCI Computations Applying the RSMBPT Method

The radial wavefunctions obtained from the above-described MCDHF calculations are used for further RCI computations, which are performed for all *OS* (OS_1, ..., OS_5) in a few ways. In the first way, RCI calculations are performed with a CSF basis constructed by applying the RSMBPT method with the same specified fraction (99.95%) as in MCDHF and including only those correlations that were included in computing radial wavefunctions. These results are marked as VV MCDHF/RCI (RSMBPT) (when only VV correlations are included in both MCDHF and RCI), VV + C MCDHF/RCI (RSMBPT) (when VV and C correlations are included in both MCDHF and RCI), VV + C + CV MCDHF/RCI (RSMBPT) (when VV, C, and CV correlations are included in both MCDHF and RCI), and VV + C + CV + CC MCDHF/RCI (RSMBPT) (when VV, C, CV, and CC correlations are included in both MCDHF and RCI). In the second way, CSFs' basis is constructed by applying the RSMBPT method with the specified fraction (99.95%) to include VV, C, CV, and CC correlations in the RCI calculations. In this case, radial wavefunctions with only chosen types of correlations included in the MCDHF are used. Such results are marked as VV MCDHF/VV + C + CV + CC RCI (RSMBPT) (when only VV correlations are included in MCDHF and VV, C, CV, and CC correlations in RCI), VV + C MCDHF/VV + C + CV + CC RCI (RSMBPT) (when VV and C correlations are included in MCDHF and VV, C, CV, and CC correlations in RCI), and VV + C + CV MCDHF/VV + C + CV + CC RCI (RSMBPT) (when VV, C, and CV correlations are included in MCDHF and VV, C, CV, and CC correlations in RCI).

5.2. Results

In this section, the results for Ar II obtained using the RSMBPT method are presented. The influence of various types of correlations was studied. The computed energy levels were compared with data from the Atomic Spectra Database (ASD) of the National Institute of Standards and Technology (NIST ASD) [43]. The E1 transitions were computed between the studied states using various computational schemes described above. The importance of correlation effects for transition data was also studied. The uncertainties of the line strengths obtained in this work were estimated based on the quantitative and qualitative evaluation (QQE) method described in [44–46].

5.2.1. Energy Level Results

As mentioned above, firstly, using the RSMBPT method, the most significant correlations with a specified fraction of 99.95% were selected for solving self-consistent field equations. Figures 12–14 show the convergence of total energies from the MCDHF (RSMBPT) computations for the three studied states. As can be seen in the figures, the contribution of C correlations does not significantly change the total energies compared with the results when only VV correlations are included (the results from the VV MCDHF (RSMBPT) and VV + C MCDHF (RSMBPT) computational schemes in these figures overlap). The energies decrease more when CV correlations are added and change the most when CC correlations are added. This behavior is independent of the configuration and term for Ar II.

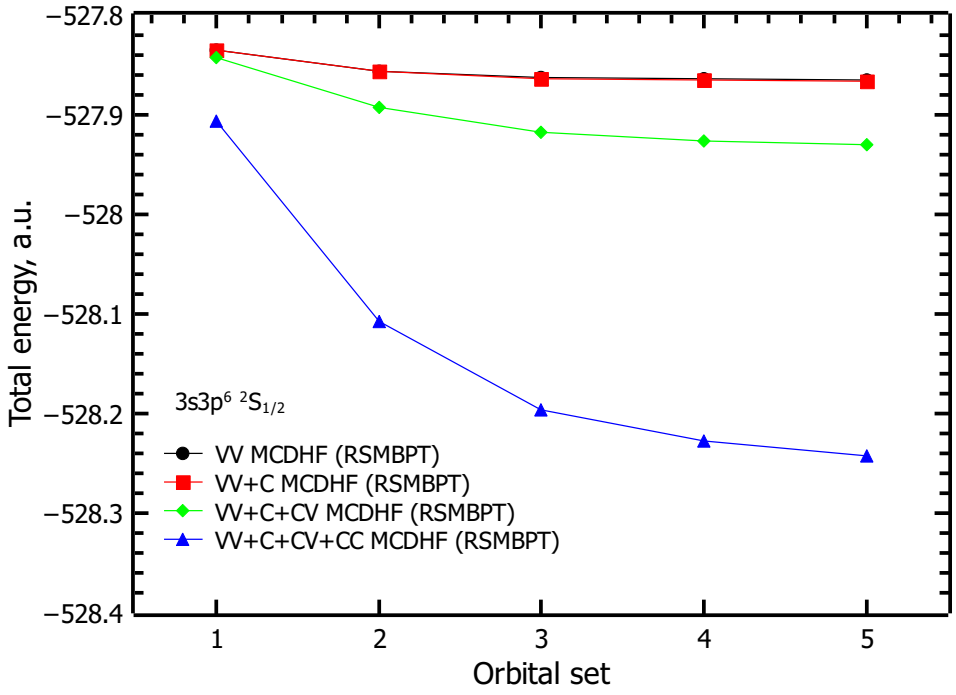

Figure 12. The convergence of the total energy of the $3s3p^6\ ^2S_{1/2}$ state when various types of correlations are included in the MCDHF (RSMBPT) computations (non-relativistic interaction) with a specified fraction of 99.95%. The results from the VV MCDHF (RSMBPT) and VV + C MCDHF (RSMBPT) computational schemes overlap.

Table 2 summarizes the CSF bases used in the RCI computations of OS_5 when the RSMBPT method with a specified fraction of 99.95% was applied. The number of CSFs is given for each computational scheme when different radial wavefunctions are used, and various types of correlations are included in the calculations. The CSF bases constructed applying the RSMBPT method, compared with those generated in the regular way, are smaller. For example, by including all correlations with the specified fraction (99.95%) in the MCDHF and RCI calculations (case VV + C + CV + CC MCDHF/RCI (RSMBPT)), the number of CSFs is 377,046 for even $J = 1/2$, 24,097 for odd $J = 1/2$, and 55,761 for odd $J = 3/2$. These CSF bases are almost twice as small as those constructed in the regular way. The number of the CSF, when the VV + C + CV + CC correlations are included at the RCI stage in the regular way, is 603,510 for even $J = 1/2$, 41,045 for odd $J = 1/2$, and 95,789 for odd $J = 3/2$.

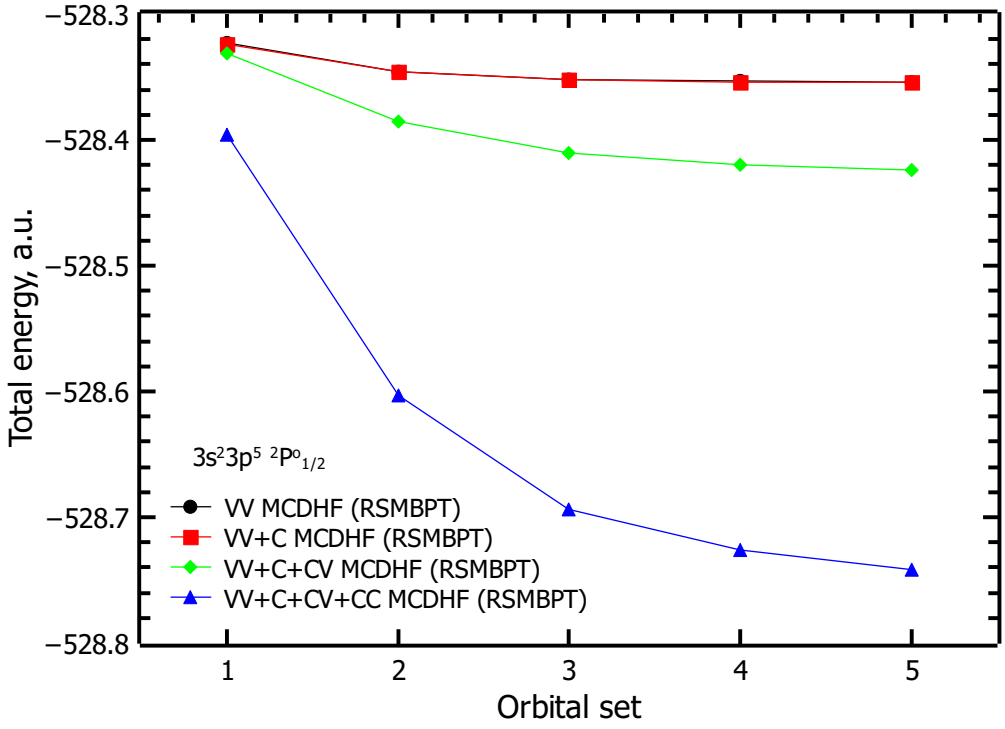

Figure 13. The convergence of the total energy of the $3s^2 3p^5\ ^2P^o_{1/2}$ state when various types of correlations are included in the MCDHF (RSMBPT) computations (non-relativistic interaction) with a specified fraction of 99.95%. The results from the VV MCDHF (RSMBPT) and VV + C MCDHF (RSMBPT) computational schemes overlap.

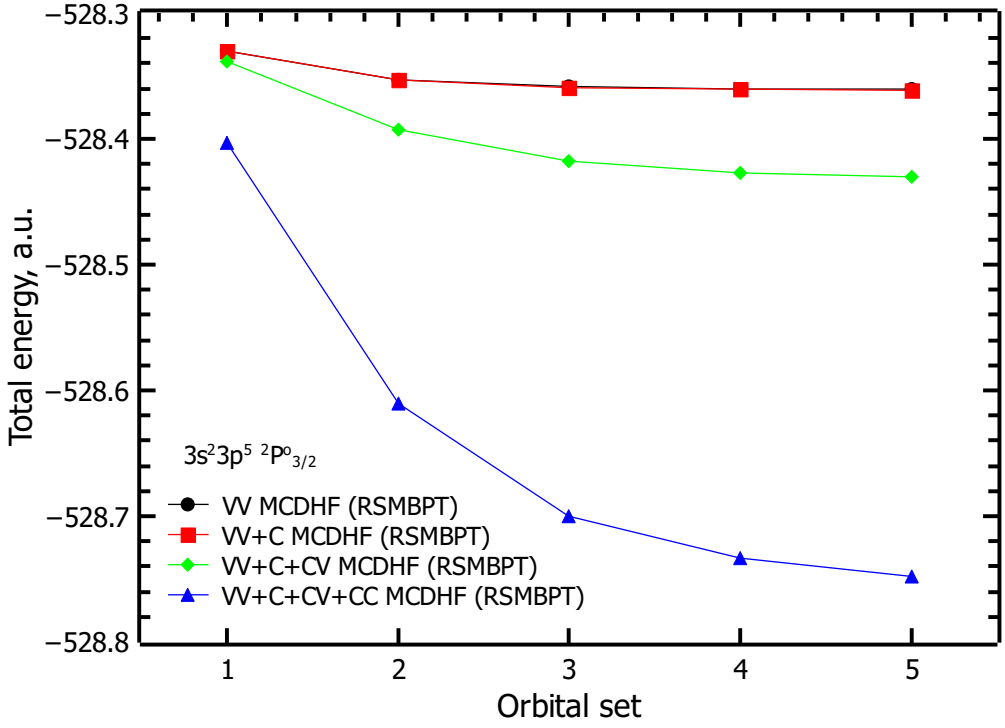

Figure 14. The convergence of the total energy of the $3s^2 3p^5\ ^2P^o_{3/2}$ state when various types of correlations are included in the MCDHF (RSMBPT) computations (non-relativistic interaction) with a specified fraction of 99.95%. The results from the VV MCDHF (RSMBPT) and VV + C MCDHF (RSMBPT) computational schemes overlap.

Table 2. Number of CSFs in the RCI computations of OS_5 using the RSMBPT method with the specified fraction (99.95%) and in the regular way.

Computational Scheme	Even J = 1/2	Odd J = 1/2	Odd J = 3/2
VV MCDHF/RCI (RSMBPT)	43,039	4136	8367
VV + C MCDHF/RCI (RSMBPT)	44,516	4112	8380
VV + C + CV MCDHF/RCI (RSMBPT)	262,109	18,781	40,262
VV MCDHF/VV + C + CV + CC RCI (RSMBPT)	433,323	27,951	63,217
VV + C MCDHF/VV + C + CV + CC RCI (RSMBPT)	433,352	27,980	63,361
VV + C + CV MCDHF/VV + C + CV + CC RCI (RSMBPT)	416,468	26,828	61,024
VV + C + CV + CC MCDHF/RCI (RSMBPT)	377,046	24,097	55,761
VV + C + CV + CC MCDHF/RCI regular	603,510	41,045	95,789

Table 3 shows at what stage of the computations the RSMBPT method was applied to select the most significant correlations. 'RSMBPT' indicates that the CSFs were constructed using the RSMBPT method (with a specified fraction of 99.95% of chosen correlations), while the mark 'regular' indicates that the CSFs were generated using the GRASP2018 package in a regular way.

Table 3. Comparison of computational schemes used in this work.

	MCDHF	RCI
MCDHF (RSMBPT)	RSMBPT	-
RCI (RSMBPT)	-	RSMBPT
MCDHF/RCI (RSMBPT)	RSMBPT	RSMBPT
MCDHF/RCI regular	RSMBPT	regular

Table 4 shows the contributions of the VV, C, CV, and CC correlations, as well as the sum of these correlations in the RCI computations using different radial wavefunctions (when different correlations applying the RSMBPT method are included to solve the self-consistent field equations). These contributions are presented for three states studied in this work: $3s3p^6\ ^2S_{1/2}$, $3s^23p^5\ ^2P^o_{1/2}$, and $3s^23p^5\ ^2P^o_{3/2}$. C correlations have the smallest contribution, while VV and CC correlations have the largest. As seen in the table, the influence of VV correlations decreases when additionally CV and CC correlations are added to MCDHF calculations. Meanwhile, the influence of CC correlations increases. As can be seen, when all correlations are included in MCDHF calculations, the total contribution of these correlations to RCI computations decreases compared with VV + C + CC cases.

Figures 15 and 16 show the convergence of energy levels using different computational schemes from RCI calculations. In these schemes, the CSFs bases are constructed by applying the RSMBPT method with the specified fraction (99.95%). The energy levels obtained using different radial wavefunctions and different types of included correlations are compared with each other and with data from the NIST ASD [43]. Filled symbols mark the results when both (MCDHF and RCI) computations include the same types of correlations. Meanwhile, empty symbols mark the results when, in the MCDHF, only some correlation types are included, and in the RCI calculations, VV, C, CV, and CC correlations are involved.

The differences between computed energy levels and the NIST results are in the range from 18 to 118 cm^{-1} for the $3s^23p^5\ ^2P^o_{1/2}$ state and from 14 to 2324 cm^{-1} for the $3s3p^6\ ^2S_{1/2}$ state. The root–mean–square (rms) deviations obtained for the computed energy levels from the NIST data are 38, 84, and 693 cm^{-1} using the following computational schemes: VV MCDHF/RCI (RSMBPT), VV + C MCDHF/RCI (RSMBPT), and VV + C + CV MCDHF/RCI (RSMBPT), respectively. By analyzing the en-

ergy levels after MCDHF calculations, the convergence trends are similar to those shown in the figures when Breit and QED corrections are added to the RCI. Depending on the correlations included in the computations, the energy levels after MCDHF are about 50–60 cm^{-1} larger for the $3s^23p^5\ ^2P^o_{1/2}$ state and about 90–100 cm^{-1} larger for the $3s3p^6\ ^2S_{1/2}$ compared with those after RCI. When all correlations are included in RCI computations, the rms deviations obtained for the computed energy levels from the NIST data are 1372, 1450, 1644, and 1582 cm^{-1}, respectively, for VV MCDHF/VV + C + CV + CC RCI (RSMBPT), VV + C MCDHF/VV + C + CV + CC RCI (RSMBPT), VV + C + CV MCDHF/VV + C + CV + CC RCI (RSMBPT), and VV + C + CV + CC MCDHF/RCI (RSMBPT).

Table 4. The contributions of correlations in the RCI computations of OS_1–OS_5 using the RSMBPT method.

Computational Scheme	VV	C	CV	CC	Total
			$3s3p^6\ ^2S_{1/2}$		
VV MCDHF/VV + C + CV + CC RCI (RSMBPT)	-3.692×10^{-1}	-7.400×10^{-3}	-9.316×10^{-2}	-2.600×10^{-1}	-7.298×10^{-1}
VV + C MCDHF/VV + C + CV + CC RCI (RSMBPT)	-3.689×10^{-1}	-7.409×10^{-3}	-9.512×10^{-2}	-2.808×10^{-1}	-7.523×10^{-1}
VV + C + CV MCDHF/VV + C + CV + CC RCI (RSMBPT)	-3.439×10^{-1}	-6.985×10^{-3}	-1.122×10^{-1}	-4.472×10^{-1}	-9.103×10^{-1}
VV + C + CV + CC MCDHF/RCI (RSMBPT)	-2.992×10^{-1}	-4.888×10^{-3}	-8.144×10^{-2}	-4.200×10^{-1}	-8.055×10^{-1}
			$3s^23p^5\ ^2P^o_{1/2}$		
VV MCDHF/VV + C + CV + CC RCI (RSMBPT)	-2.340×10^{-1}	-7.713×10^{-3}	-8.675×10^{-2}	-2.599×10^{-1}	-5.884×10^{-1}
VV + C MCDHF/VV + C + CV + CC RCI (RSMBPT)	-2.337×10^{-1}	-7.722×10^{-3}	-8.888×10^{-2}	-2.808×10^{-1}	-6.111×10^{-1}
VV + C + CV MCDHF/VV + C + CV + CC RCI (RSMBPT)	-2.094×10^{-1}	-7.306×10^{-3}	-1.048×10^{-1}	-4.466×10^{-1}	-7.681×10^{-1}
VV + C + CV + CC MCDHF/RCI (RSMBPT)	-1.620×10^{-1}	-5.076×10^{-3}	-7.516×10^{-2}	-4.194×10^{-1}	-6.616×10^{-1}
			$3s^23p^5\ ^2P^o_{3/2}$		
VV MCDHF/VV + C + CV + CC RCI (RSMBPT)	-2.232×10^{-1}	-7.173×10^{-3}	-8.644×10^{-2}	-2.599×10^{-1}	-5.767×10^{-1}
VV + C MCDHF/VV + C + CV + CC RCI (RSMBPT)	-2.229×10^{-1}	-7.196×10^{-3}	-8.853×10^{-2}	-2.808×10^{-1}	-5.994×10^{-1}
VV + C + CV MCDHF/VV + C + CV + CC RCI (RSMBPT)	-1.988×10^{-1}	-6.815×10^{-3}	-1.043×10^{-1}	-4.466×10^{-1}	-7.566×10^{-1}
VV + C + CV + CC MCDHF/RCI (RSMBPT)	-1.516×10^{-1}	-4.765×10^{-3}	-7.483×10^{-2}	-4.193×10^{-1}	-6.506×10^{-1}

Tables 5 and 6 present a comparison of results obtained using the MCDHF/RCI (RSMBPT) computational schemes, including different types of correlations with the results from regular computations, (when radial wavefunctions were taken from MCDHF (RSMBPT) and a CSF basis was constructed in the regular way at the RCI stage). For this purpose, additional computations at the RCI (RSMBPT) stage using 100% specified fraction [15] and regular computations were performed. Table 5 shows the comparison of the total energies, while Table 6 presents a comparison of the energy levels for the studied states at OS_5. It is seen that the developed MCDHF/RCI (RSMBPT) method works perfectly when the chosen types of correlations are taken into account using the RSMBPT method, and the results reproduce the regular GRASP2018 data.

As was observed in [15,17], the dependence of the contribution of included correlations on the specified fraction of the total correlation contribution used in the RCI (RSMBPT) method is linear. This dependence was also checked in this work. For this purpose, additional computations at the RCI (RSMBPT) stage using other specified fractions: 95, 99, 99.5, 99.95, and 100% were performed. Table 7 presents the contribution of the included correlations (Δ_{cor}) using the RCI (RSMBPT) method compared with complete regular RCI computations for the $3s^23p^5\ ^2P^o_{3/2}$ state. The contribution, Δ_{cor} (in %), is computed according to the $(TE_{RCI\ (RSMBPT)} - TE_{MR+})/(TE_{RCI} - TE_{MR+})$ [15], where TE represents the total energy from a certain computational scheme. $TE_{RCI\ (RSMBPT)}$ is the total energy from the RCI (RSMBPT) method using the specified fraction (in %) of the total correlations' contribution. The MR+ results are from computations in which the CSFs' basis consists of the MR set, along with the correlations that were not included by applying the RSMBPT method. As seen from the table, the computed Δ_{cor} is almost identical to the specified

fraction (in %) of the total correlation contribution used in the RCI (RSMBPT) method. There are some larger differences when radial wavefunctions and calculations were included in CV and CC correlations. The same trends of dependence were obtained for the remaining two states that were studied in this work.

Table 5. The total energies (in a.u.) for $3s^2 3p^5\ ^2P^o_{3/2}$, $3s^2 3p^5\ ^2P^o_{1/2}$, and $3s3p^6\ ^2S_{1/2}$ states from VV MCDHF/VV + C + CV + CC RCI (RSMBPT), VV + C MCDHF/VV + C + CV + CC RCI (RSMBPT), VV + C + CV MCDHF/VV + C + CV + CC RCI (RSMBPT), and VV + C + CV + CC MCDHF/RCI (RSMBPT) computational schemes compared with results from regular computations.

Computational Scheme	$3s^2 3p^5\ ^2P^o_{3/2}$	$3s^2 3p^5\ ^2P^o_{1/2}$	$3s3p^6\ ^2S_{1/2}$
VV MCDHF/VV + C + CV + CC RCI regular	−528.41024839	−528.40346015	−527.90603684
VV MCDHF/VV + C + CV + CC RCI (RSMBPT) 100%	−528.41024818	−528.40345994	−527.90603649
VV MCDHF/VV + C + CV + CC RCI (RSMBPT) 99.95%	−528.40990389	−528.40311213	−527.90569310
VV + C MCDHF/VV + C + CV + CC RCI regular	−528.43013256	−528.42337001	−527.92541736
VV + C MCDHF/VV + C + CV + CC RCI (RSMBPT) 100%	−528.43013250	−528.42336997	−527.92541713
VV + C MCDHF/VV + C + CV + CC RCI (RSMBPT) 99.95%	−528.42975757	−528.42297982	−527.92504172
VV + C + CV MCDHF/VV + C + CV + CC RCI regular	−528.52044582	−528.51373335	−528.01392204
VV + C + CV MCDHF/VV + C + CV + CC RCI (RSMBPT) 100%	−528.52044482	−528.51373286	−528.01392059
VV + C + CV MCDHF/VV + C + CV + CC RCI (RSMBPT) 99.95%	−528.51775243	−528.51114510	−528.01178752
VV + C + CV + CC MCDHF/RCI regular	−528.54094069	−528.53432631	−528.03480323
VV + C + CV + CC MCDHF/RCI (RSMBPT) 100%	−528.54091141	−528.53430070	−528.03479217
VV + C + CV + CC MCDHF/RCI (RSMBPT) 99.95%	−528.53577634	−528.52951408	−528.03021099

Table 6. Energy levels (in cm^{-1}) for $3s^2 3p^5\ ^2P^o_{1/2}$ and $3s3p^6\ ^2S_{1/2}$ states from VV MCDHF/VV + C + CV + CC RCI (RSMBPT), VV + C MCDHF/VV + C + CV + CC RCI (RSMBPT), VV + C + CV MCDHF/VV + C + CV + CC RCI (RSMBPT), and VV + C + CV + CC MCDHF/RCI (RSMBPT) computational schemes compared with results from regular computations.

Computational Scheme	$3s^2 3p^5\ ^2P^o_{1/2}$	$3s3p^6\ ^2S_{1/2}$
VV MCDHF/VV + C + CV + CC RCI regular	1489.85	110,661.65
VV MCDHF/VV + C + CV + CC RCI (RSMBPT) 100%	1489.85	110,661.67
VV MCDHF/VV + C + CV + CC RCI (RSMBPT) 99.95%	1490.62	110,661.48
VV + C MCDHF/VV + C + CV + CC RCI regular	1484.21	110,772.18
VV + C MCDHF/VV + C + CV + CC RCI (RSMBPT) 100%	1484.20	110,772.22
VV + C MCDHF/VV + C + CV + CC RCI (RSMBPT) 99.95%	1487.54	110,772.33
VV + C + CV MCDHF/VV + C + CV + CC RCI regular	1473.22	111,169.12
VV + C + CV MCDHF/VV + C + CV + CC RCI (RSMBPT) 100%	1473.11	111,169.22
VV+C+CV MCDHF/VV + C + CV + CC RCI (RSMBPT) 99.95%	1450.14	111,046.46
VV + C + CV + CC MCDHF/RCI regular	1451.69	111,084.33
VV + C + CV + CC MCDHF/RCI (RSMBPT) 100%	1450.88	111,080.33
VV + C + CV + CC MCDHF/RCI (RSMBPT) 99.95%	1374.41	110,958.77

Table 7. The contribution of included correlations (Δ_{cor} (in %)) using the RCI (RSMBPT) method compared with the regular RCI computations for the $3s^2 3p^5\ ^2P^o_{3/2}$ state.

	Specified Fraction in the RCI (RSMBPT)				
	95%	**99%**	**99.5%**	**99.95%**	**100%**
VV MCDHF/VV + C + CV + CC RCI (RSMBPT)	95.117	98.943	99.410	99.918	100.000
VV + C MCDHF/VV + C + CV + CC RCI (RSMBPT)	95.112	98.940	99.408	99.915	100.000
VV + C + CV MCDHF/VV + C + CV + CC RCI (RSMBPT)	93.959	97.852	98.517	99.493	100.000
VV + C + CV + CC MCDHF/RCI (RSMBPT)	91.028	95.984	97.189	99.065	99.995

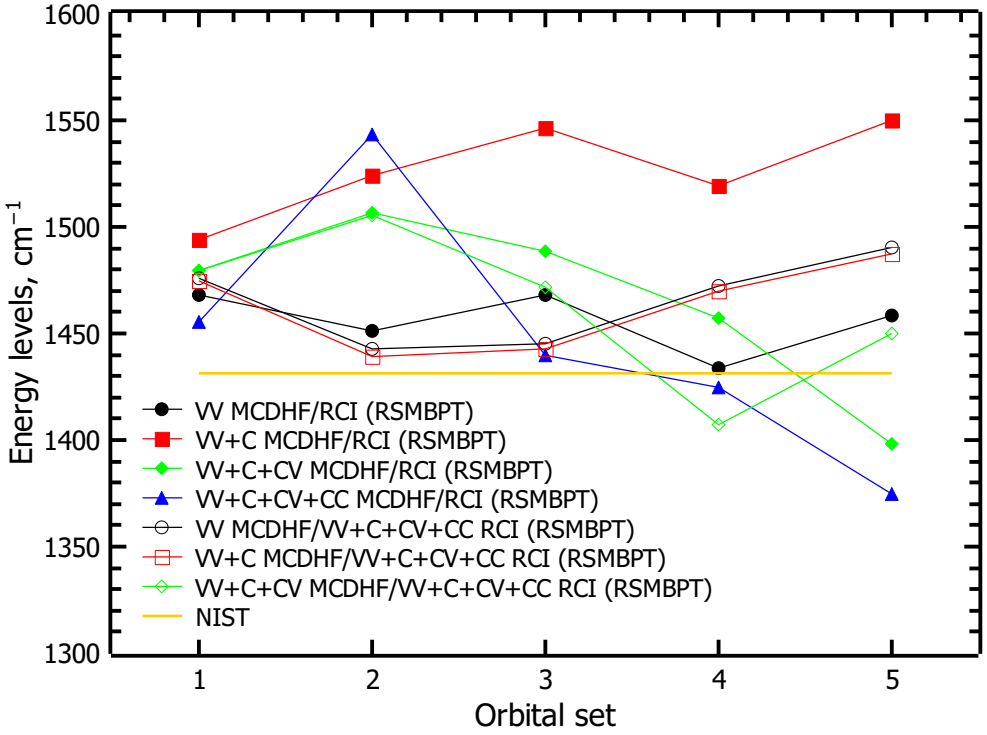

Figure 15. The convergence of the energy level of the $3s^2 3p^5\ ^2P^o_{1/2}$ when various types of correlations are included in the RCI computations (non-relativistic, Breit, and QED).

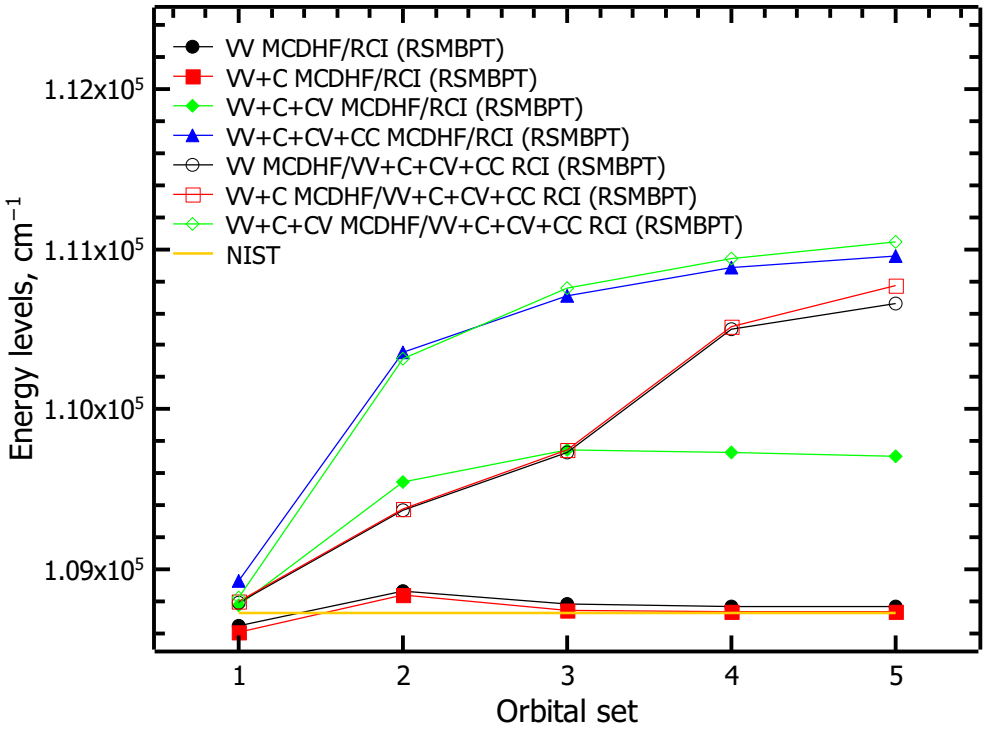

Figure 16. The convergence of the energy level of the $3s3p^6\ ^2S_{1/2}$ when various types of correlations are included in the RCI computations (non-relativistic, Breit, and QED).

The disagreements between the computed Δ_{cor} and the specified fraction used in the RCI (RSMBPT) method, in addition to those mentioned previously in [15], could be related to the following: (i) the average energy in the denominator of the Feynman diagram expression is used instead of the energy from the theory; (ii) the contribution of correlation is computed for the configuration (occupation of the relativistic subshells

without intermediate term), but not for the ASF (configuration with intermediate terms); (iii) the duplication of CSFs that are in both (MR+ and PT) lists. As mentioned in Section 5.1, the correlations (Equations (26) and (27)), which cannot be estimated with the RSMBPT method, were added to calculations in a regular way. These CSFs were generated using the 'rcsfgenarate' program [9], in which single substitutions were allowed from the valence or core shell. Using the PT theory, correlations are estimated by the subshells. Therefore, some CSFs generated in a regular way can duplicate these estimates, applying PT theory. This duplication is checked and removed in the atomic calculations. However, computing the contribution Δ_{cor} this duplication remains what could cause the small discrepancy.

5.2.2. Transition Results

Figures 17 and 18 present the convergence of the line strengths of the $3s3p^6\ ^2S_{1/2}$–$3s^23p^5\ ^2P^o_{1/2}$ and $3s3p^6\ ^2S_{1/2}$–$3s^23p^5\ ^2P^o_{3/2}$ transitions using different computational schemes described above. The results marked as 'symbols and straight line' show the results when the same types of correlations are included in both the MCDHF and RCI computations. 'Symbols and dashed line' mark the results when only some correlation types are included in the MCDHF and VV, C, CV, and CC correlations are involved in the RCI calculations. Filled symbols mark the line strengths in the Babushkin gauge, while empty symbols mark results in the Coulomb gauge. At the last step in the transition parameters calculations, the experimental transition energy was applied; these results are marked as 'En. adj.'.

It can be seen that the values of the line strengths can vary significantly when the results of two computations with the same radial wavefunctions but different types of correlations included at the RCI stage are compared. This is especially evident when only VV or VV + C correlations are included in the computations. The largest changes occur in the line strengths in the Coulomb gauge. Line strengths in the Babushkin gauge are less sensitive to the included correlations.

By analyzing the agreement between the two gauges, the accuracy of the line strength for the $3s3p^6\ ^2S_{1/2}$–$3s^23p^5\ ^2P^o_{1/2}$ transition at the final OS_5 varies between the B and AA accuracy classes, depending on the strategy used in the calculations. The AA accuracy class is achieved when all (VV, C, CV, and CC) correlations are included in the RCI calculations. By applying the experimental transition energy to the transition data calculations, the accuracy of the line strength for this transition is evaluated as B+. The accuracy of the line strength for the $3s3p^6\ ^2S_{1/2}$–$3s^23p^5\ ^2P^o_{3/2}$ transition at the final OS_5 is estimated as D+. The accuracy class of this transition remains D+ when the experimental transition energy is used to calculate the transition parameters. Unlike the line strength in the Coulomb gauge, the line strength in the Babushkin gauge does not change when the experimental transition energy is applied to the transition data calculations.

In Figures 17 and 18, the line strengths from the NIST database are also shown; they are marked by a yellow, straight line. These line strengths for two transitions are evaluated in the NIST with a C ($\leq$25%) accuracy class; the uncertainties for these lines are marked as yellow, dotted lines. By comparing these line strengths with the computed ones, it is seen that they are closer to the line strengths when only VV or VV + C correlations are included in the MCDHF and RCI computations. The computed line strengths in both gauges for the $3s3p^6\ ^2S_{1/2}$–$3s^23p^5\ ^2P^o_{1/2}$ transition obtained using the VV MCDHF/RCI (RSMBPT) and VV + C MCDHF/RCI (RSMBPT) schemes fall within the uncertainty limits of the line strengths given by the NIST. For the $3s3p^6\ ^2S_{1/2}$–$3s^23p^5\ ^2P^o_{3/2}$ transition, the line strengths in the Babushkin gauge from all computational schemes, as well as the line strengths in the Coulomb gauge from the VV MCDHF/RCI (RSMBPT) and VV + C + CV MCDHF/RCI (RSMBPT) computational schemes, fall within the uncertainty limits of the line strengths given by the NIST.

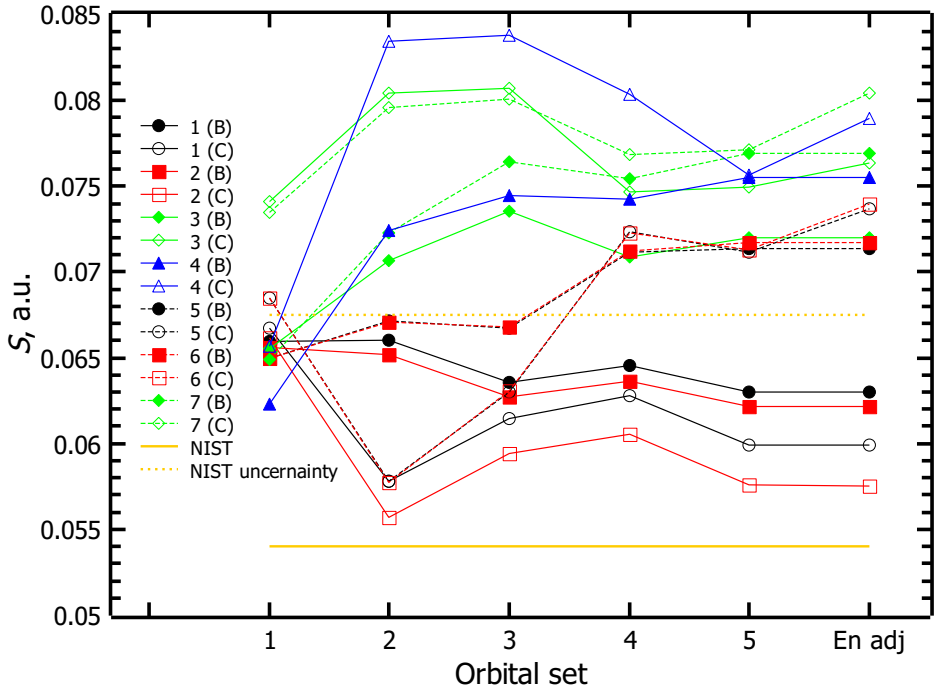

Figure 17. The convergence of the line strength of the $3s3p^6\ ^2S_{1/2}$–$3s^23p^5\ ^2P^o_{1/2}$ transition using different computational schemes. The computational schemes in the legend are marked: 1—VV MCDHF/RCI (RSMBPT); 2—VV + C MCDHF/RCI (RSMBPT); 3—VV + C + CV MCDHF/RCI (RSMBPT); 4—VV + C + CV + CC MCDHF/RCI (RSMBPT); 5—VV MCDHF/VV + C + CV + CC RCI (RSMBPT); 6—VV + C MCDHF/VV + C + CV + CC RCI (RSMBPT); 7—VV + C + CV MCDHF/VV + C + CV + CC RCI (RSMBPT). The line strengths are presented in the Babushkin (B) and Coulomb (C) gauges.

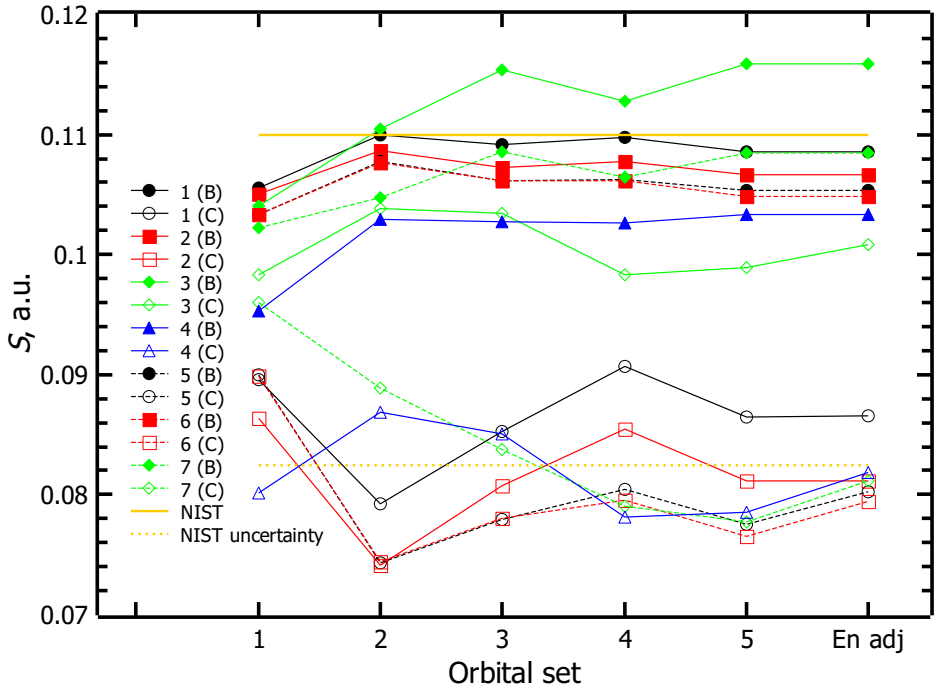

Figure 18. The convergence of the line strength of the $3s3p^6\ ^2S_{1/2}$–$3s^23p^5\ ^2P^o_{3/2}$ transition using different computational schemes. The computational schemes in the legend are marked: 1—VV MCDHF/RCI (RSMBPT); 2—VV + C MCDHF/RCI (RSMBPT); 3—VV + C + CV MCDHF/RCI (RSMBPT); 4—VV + C + CV + CC MCDHF/RCI (RSMBPT); 5—VV MCDHF/VV + C + CV + CC RCI (RSMBPT); 6—VV + C MCDHF/VV + C + CV + CC RCI (RSMBPT); 7—VV + C + CV MCDHF/VV + C + CV + CC RCI (RSMBPT). The line strengths are presented in the Babushkin (B) and Coulomb (C) gauges.

5.2.3. Lifetime Results

The lifetime of the $3s3p^6\ ^2S_{1/2}$ state was computed in the Babushkin and Coulomb gauges using the abovementioned computational schemes. These results are presented in Table 8 and compared with the experimental results (marked as 'Ex.') and other theoretical results (marked as 'Th.'). The column labeled as 'En. adj.' in the table presents the lifetimes when the experimental transition energy was applied to the transition parameters calculations. The lifetime in the NIST row of the table was computed using the transition rates given in the NIST database.

Table 8. Comparison of the computed lifetimes (in ns) for the $3s3p^6\ ^2S_{1/2}$ state with the experimental and theoretical results. The lifetimes are given in the Babushkin (B) and Coulomb (C) gauges. 'En. adj.' means that in the transition parameters calculations, the experimental transition energy was applied.

Computational Scheme	OS_5		En. adj.	
	B	C	B	C
VV MCDHF/RCI (RSMBPT)	4.536	5.327	4.541	5.328
VV + C MCDHF/RCI (RSMBPT)	4.623	5.632	4.619	5.630
VV + C + CV MCDHF/RCI (RSMBPT)	4.038	4.370	4.150	4.410
VV MCDHF/VV + C + CV + CC RCI (RSMBPT)	4.190	4.996	4.417	5.084
VV + C MCDHF/VV + C + CV + CC RCI (RSMBPT)	4.181	5.010	4.421	5.104
VV + C + CV MCDHF/VV + C + CV + CC RCI (RSMBPT)	3.951	4.746	4.211	4.848
VV + C + CV + CC MCDHF/RCI (RSMBPT)	4.104	4.771	4.367	4.871
Ex. [47]	4.62 ± 0.045			
Ex. [48]	4.684 ± 0.019			
NIST [43]	4.83			
Th. [47] in the B gauge	4.66			
Th. [47] in the C gauge	5.37			
Th. [49]	4.291			

The lifetimes in the Babushkin gauge, adjusted by the experimental transition energy, agree well with the experimental results [47,48] and other theoretical results [47,49]. In this case, the lifetimes from the VV MCDHF/RCI (RSMBPT) and VV + C MCDHF/RCI (RSMBPT) strategies agree very well with the experimental results. However, the agreement between the two gauges is not as good. For the remaining strategies, the agreement between the Babushkin and Coulomb gauges improves. By comparing the lifetimes adjusted by the experimental transition energy with the experimental ones [47,48] and at the same time evaluating the agreement between the two gauges, the VV + C + CV + CC MCDHF/RCI (RSMBPT) strategy demonstrates good agreement.

6. Conclusions

By generalizing the method developed by our group, the extension of the approach presented in this paper allows us to achieve the next level of application for more general cases and essentially completes the methodology. This approach can also be successfully applied to the regular Rayleigh–Schrödinger many-body perturbation theory; however, it should be noted that the radial part of regular perturbation theory is beyond the scope of the present paper.

The developed method, based on the Rayleigh–Schrödinger perturbation theory in an irreducible tensorial form, allows estimation of the CV, C, CC, and VV correlations. The contribution of these correlations can be investigated for any atom or ion with an arbitrary number of valence and core electrons. This paper presents all the Feynman diagrams that describe these correlations together with the analytical expressions of these diagrams

derived in an irreducible tensorial form. It also provides rules for obtaining algebraic expressions of any Feynman diagram in this form.

This newly developed method can be used in three ways: (i) RCI + RSMBPT; (ii) RCI (RSMBPT); and (iii) MCDHF (RSMBPT). The RSMBPT method can be applied to MCDHF and RCI computations, choosing the same types of correlations as well as different types of correlations in both computations. Selecting the most important correlations with the RSMBPT method allows reducing the space of configuration state functions and including correlations in a systematic way. This is especially useful and beneficial for calculations involving complex atoms and ions. Such benefits of the RSMBPT method over the regular method extend the capability of the GRASP2018 software package. The application of the RSMBPT method for atomic calculations in different ways is presented in this work.

Author Contributions: Theory and programming, G.G.; testing program, P.R. and L.K.; calculation, P.R. and L.K.; discussion and theory validation, G.G., P.R. and L.K.; writing—original draft, G.G., P.R. and L.K.; writing—review and editing G.G., P.R. and L.K. All authors have read and agreed to the published version of the manuscript.

Funding: This research received no external funding.

Data Availability Statement: The data that support the findings of this study are available from the corresponding author upon reasonable request.

Conflicts of Interest: The authors declare no conflicts of interest.

Abbreviations

The following abbreviations are used in this manuscript:

GRASP	General Relativistic Atomic Structure package
GRASP2018	Latest GRASP program package version
GRASP2018_PT	Extension of the GRASP2018 software package in a combination of MCDHF, RCI, and RSMBPT in the irreducible tensorial form
ASF	Atomic state function
CSF	Configuration state function
MCDHF	Multiconfiguration Dirac–Hartree–Fock
RCI	Relativistic configuration interaction
RME	Reduced matrix element
RSMBPT	Rayleigh–Schrödinger many-body perturbation theory
CV	Core–valence
CC	Core–core
C	Core
VV	Valence–valence
MCDHF (RSMBPT)	RSMBPT is applied in the MCDHF computations
RCI (RSMBPT)	RSMBPT is applied in the RCI computations
MCDHF/RCI (RSMBPT)	RSMBPT is applied in both MCDHF and RCI computations
<type>MCDHF/RCI (RSMBPT)	RSMBPT is applied in both MCDHF and RCI computations, including the chosen <type> of correlations, which is the same for both computations. For example, VV + C MCDHF/RCI (RSMBPT) means that VV and C correlations were included in both MCDHF and RCI computations applying RSMBPT method
<type1>MCDHF/ <type2>RCI (RSMBPT)	RSMBPT is applied in both MCDHF and RCI computations, including <type1> of correlations in the MCDHF computations and <type2> of correlations in the RCI computations
MR	Multireference
QED	Quantum electrodynamic corrections

OS	Orbital set
QQE	Quantitative and qualitative evaluation method

Appendix A. The Reduced Matrix Element of Triple Tensors

This appendix presents the specifics of calculating the reduced matrix elements (RME) listed below in the stationary second-order Rayleigh–Schrödinger many-body perturbation theory in an irreducible tensorial form [12–17].

$$\mathrm{RME}_A \equiv \left\langle \Psi \left\| \left[\left[\tilde{a}^{(j)} \times a^{(j)} \right]^{(k)} \times \left[\left[a^{(j')} \times \tilde{a}^{(j')} \right]^{(x)} \times \left[a^{(j')} \times \tilde{a}^{(j')} \right]^{(k')} \right]^{(k)} \right]^{(0)} \right\| \Psi \right\rangle, \tag{A1}$$

$$\mathrm{RME}_B \equiv \left\langle \Psi \left\| \left[\left[\left[\tilde{a}^{(j)} \times a^{(j)} \right]^{(k)} \times \left[a^{(j'')} \times \tilde{a}^{(j'')} \right]^{(x)} \right]^{(k')} \times \left[a^{(j')} \times \tilde{a}^{(j')} \right]^{(k')} \right]^{(0)} \right\| \Psi \right\rangle, \tag{A2}$$

$$\mathrm{RME}_C \equiv \left\langle \Psi \left\| \left[\left[a^{(j)} \times \tilde{a}^{(j)} \right]^{(k)} \times \left[\left[a^{(j')} \times \tilde{a}^{(j')} \right]^{(x)} \times \left[\tilde{a}^{(j')} \times a^{(j')} \right]^{(k')} \right]^{(k)} \right]^{(0)} \right\| \Psi \right\rangle, \tag{A3}$$

$$\mathrm{RME}_D \equiv \left\langle \Psi \left\| \left[\left[\left[a^{(j)} \times \tilde{a}^{(j)} \right]^{(k)} \times \left[\tilde{a}^{(j'')} \times a^{(j'')} \right]^{(x)} \right]^{(k')} \times \left[\tilde{a}^{(j')} \times a^{(j')} \right]^{(k')} \right]^{(0)} \right\| \Psi \right\rangle, \tag{A4}$$

where

$$\| \Psi \rangle \equiv \left\| 3\mathrm{s}^2\, 3\mathrm{p}_-\, 3\mathrm{p}^3\, (J_{23} = 2)\, 3\mathrm{d}\; J = \frac{1}{2} \right\rangle.$$

RME_A and RME_B reduced matrix elements come from the triple VV_3 Feynman diagram (see Figure 1), and RME_C and RME_D reduced matrix elements come from the triple CV_7 Feynman diagram (see Figure 1). Table A1 presents the values of these reduced matrix elements (see Value column) for specific combinations of second quantization operators acting on subshells (see columns $a^{(j)}$, $a^{(j')}$, and $a^{(j'')}$) and for certain values of the tensorial product ranks k, k', and x (see columns k, k', and x). The last column of the table lists the second quantization operators that form the energy multiplier D (28) of the Feynman diagrams under consideration and that belong to the F' space. The examples in the table illustrate certain peculiarities of calculating reduced matrix elements (A1) and (A2) in the stationary second-order Rayleigh–Schrödinger many-body perturbation theory in an irreducible tensorial form, which we will now discuss.

Table A1. Values of RME_A, RME_B, RME_C, and RME_D reduced matrix elements (a test case).

RME	$a^{(j)}$	$a^{(j')}$	$a^{(j'')}$	k	k'	x	Value	The Second Quantization Operators for D (28)
RME_A	$3\mathrm{p}_-$	$3\mathrm{p}^3$	–	1	1	1	0.0866025	$a^{(j)}, \tilde{a}^{(j')}, \tilde{a}^{(j')}$
RME_A	$3\mathrm{p}_-$	$3\mathrm{p}^3$	–	1	2	2	−0.1936492	$a^{(j)}, \tilde{a}^{(j')}, \tilde{a}^{(j')}$
RME_A	$3\mathrm{p}_-$	$3\mathrm{p}^3$	–	1	2	3	0.1620185	$a^{(j)}, \tilde{a}^{(j')}, \tilde{a}^{(j')}$
RME_B	$3\mathrm{p}_-$	$3\mathrm{d}$	$3\mathrm{p}^3$	1	1	0	0.5123475	$a^{(j)}, \tilde{a}^{(j')}, \tilde{a}^{(j'')}$
RME_B	$3\mathrm{d}$	$3\mathrm{p}_-$	$3\mathrm{s}^2$	1	1	0	0.4830459	$a^{(j)}, \tilde{a}^{(j')}, \tilde{a}^{(j'')}$
RME_B	$3\mathrm{p}_-$	$3\mathrm{d}$	$3\mathrm{p}^3$	1	4	3	0.3162278	$a^{(j)}, \tilde{a}^{(j')}, \tilde{a}^{(j'')}$
RME_C	$3\mathrm{p}_-$	$3\mathrm{d}$	–	1	1	1	−0.0577350	$a^{(j')}, a^{(j')}, \tilde{a}^{(j)}$
RME_C	$3\mathrm{p}_-$	$3\mathrm{d}$	–	1	2	2	−0.1290994	$a^{(j')}, a^{(j')}, \tilde{a}^{(j)}$
RME_C	$3\mathrm{p}_-$	$3\mathrm{d}$	–	1	2	3	−0.2121320	$a^{(j')}, a^{(j')}, \tilde{a}^{(j)}$
RME_D	$3\mathrm{p}_-$	$3\mathrm{d}$	$3\mathrm{p}^3$	1	1	0	−0.1707825	$a^{(j')}, a^{(j'')}, \tilde{a}^{(j)}$
RME_D	$3\mathrm{d}$	$3\mathrm{p}_-$	$3\mathrm{s}^2$	1	1	0	0.0000000	$a^{(j')}, a^{(j'')}, \tilde{a}^{(j)}$
RME_D	$3\mathrm{p}_-$	$3\mathrm{d}$	$3\mathrm{p}^3$	1	4	3	0.3162278	$a^{(j')}, a^{(j'')}, \tilde{a}^{(j)}$

- Table A1 presents different sets of second quantization operators acting on the subshells for RME_A and RME_C. In the RME_A case, the operators $a^{(j)}$ and $a^{(j')}$ act on the $3p_-$ and $3p^3$ subshells, respectively, while in the RME_C case, they act on the $3p_-$ and 3d subshells. These cases have been specifically chosen because, as already mentioned, RME_A and RME_C originate from different Feynman diagrams. Therefore, if we consider the RME_C case with the operators $a^{(j)}$ and $a^{(j')}$ acting on the $3p_-$ and $3p^3$ subshells, the reduced matrix element will be non-zero, even though the Feynman diagram CV_7 itself is zero. This zero value results from energy multiplier D, which is zero, $D = 0$; i.e., when two creation operators $a^{(j')}$ (see the last column of Table A1) act on the $3p_-$ subshell, three electrons should appear there, but according to atomic theory, the maximum number of electrons in this subshell can only be two. Therefore, although the reduced matrix elements themselves are non-zero, they do not need to be calculated using the current methodology. For the same reason, the RME_A, which involves the second quantization operators $a^{(j)}$ and $a^{(j')}$ (see the last column of Table A1) acting on the $3p_-$ and 3d subshells, also does not need to be calculated. In this case, D from VV_3 will be zero as well, since the two annihilation operators $\tilde{a}^{(j')}$ acting on the 3d subshell with a single electron will yield zero.
- In some cases, it is possible to determine immediately, without calculation, whether a reduced matrix element is zero or not. For example, in the case of RME_B, when the second quantization operators $a^{(j)}$, $a^{(j')}$, and $a^{(j'')}$ (see the last column of Table A1) act on the 3d, $3p_-$, and $3s^2$ orbitals and have ranks $k = 1$, $k' = 1$, and $x = 0$, respectively, the RME_B is non-zero ($RME_B = 0.4830459$), but with the same values, the RME_D is zero. This can be easily determined because, when calculating the reduced matrix element, the creation operator $a^{(j'')}$ (see the last column of Table A1) acts on a closed shell (in our case $3s^2$); thus, according to the theory of second quantization, it is equal to zero (see the second line of the RME_D in Table A1).
- Special attention should be drawn to the values of RME_B and RME_D presented in the table, which are equal ($RME_B = 0.3162278$ and $RME_D = 0.3162278$) even though the tensorial structures of their respective operators differ. Such cases, where the values of the reduced matrix elements (A1)–(A4) are the same, can be easily explained using a well-known commutation rule of second quantization (see, for example, (29) from [36], where the expression is in *LS*-coupling)

$$\left[\tilde{a}^{(j_i)} \times a^{(j_k)}\right]^{(x)} = -(-1)^{j_i+j_k-x} \left[a^{(j_k)} \times \tilde{a}^{(j_i)}\right]^{(x)} + \sqrt{[j_i]}\, \delta(n_i l_i j_i, n_k l_k j_k)\, \delta(x, 0). \quad \text{(A5)}$$

When the rank x of these operators is not zero, this expression will take the following form:

$$\left[\tilde{a}^{(j_i)} \times a^{(j_k)}\right]^{(x\neq 0)} = -(-1)^{j_i+j_k-x} \left[a^{(j_k)} \times \tilde{a}^{(j_i)}\right]^{(x\neq 0)}. \quad \text{(A6)}$$

The tensorial structure present in the reduced matrix element RME_B—in our case, when $k = 1$, $k' = 4$, and $x = 3$—can be transformed into the tensorial structure present in RME_D by applying relation (A6) three times to the pairs of operators $\left[\tilde{a}^{(j=\frac{1}{2})} \times a^{(j=\frac{1}{2})}\right]^{(k=1)}$, $\left[a^{(j''=\frac{3}{2})} \times \tilde{a}^{(j''=\frac{3}{2})}\right]^{(x=3)}$, and $\left[a^{(j'=\frac{5}{2})} \times \tilde{a}^{(j'=\frac{5}{2})}\right]^{(k'=4)}$ from (A2). From this, we can see that the values of these matrix elements are equal, since

$$\left[\left[\left[\tilde{a}^{(j=\frac{1}{2})} \times a^{(j=\frac{1}{2})}\right]^{(k=1)} \times \left[a^{(j''=\frac{3}{2})} \times \tilde{a}^{(j''=\frac{3}{2})}\right]^{(x=3)}\right]^{(k'=4)} \times \left[a^{(j'=\frac{5}{2})} \times \tilde{a}^{(j'=\frac{5}{2})}\right]^{(k'=4)}\right]^{(0)}$$

$$= \left[\left[\left[a^{(j=\frac{1}{2})} \times \tilde{a}^{(j=\frac{1}{2})}\right]^{(k=1)} \times \left[\tilde{a}^{(j''=\frac{3}{2})} \times a^{(j''=\frac{3}{2})}\right]^{(x=3)}\right]^{(k'=4)} \times \left[\tilde{a}^{(j'=\frac{5}{2})} \times a^{(j'=\frac{5}{2})}\right]^{(k'=4)}\right]^{(0)}. \quad \text{(A7)}$$

Equation (A5) can also explain why RME_B and RME_D have different values ($\mathrm{RME}_B = 0.5123475$ and $\mathrm{RME}_D = -0.1707825$) for the ranks $k = 1$, $k' = 1$, and $x = 0$. Furthermore, based on (A6), it is possible to identify cases where the reduced matrix elements have opposite signs.

All of the rules listed above are general and apply to (A1)–(A4).

Appendix B. The Subroutine `WW1`

The subroutine determines the value of the matrix elements (48).

The subroutine has the following arguments:

1. `IK` is the array `I` (see Section 3.3 in [20]) for the bra function.
2. `BK` is the array `B` (see Section 3.3 in [20]) for the bra function.
3. `ID` is the array `I` for the ket function.
4. `BD` is the array `B` for the ket function.
5. `K1` is the rank x.
6. `K2` is the rank J_2.
7. `K` is the rank J_1.
8. `QM1`, `QM2`, `QM3`, and `QM4` are the quasi-spin projections in (48).
9. `WW` is the value of the reduced matrix element (48), which is returned by the subroutine.

Table A2 presents three test cases for the subroutine `WW1G`. They are taken for estimation of the CV and VV correlations, described by the three-particle Feynman diagram, using the Rayleigh–Schrödinger perturbation theory in an irreducible tensorial form. For this purpose, the levels of the $3s^2 3p^4 3d$ configuration of Ar II are studied. In the calculations, the 1s, 2s, $2p_-$, and 2p subshells are defined as core subshells (that correspond to the F set); the 3s, $3p_-$, 3p, $3d_-$, and 3d subshells are defined as valence subshells (that correspond to the F' set). The 4s, $4p_-$, 4p, $4d_-$, 4d, $4f_-$, 4f subshells are defined as virtual ones (that correspond to the G set).

Table A2. The input and output argument values for the subroutine `WW1G` in the test cases.

No.	IK	ID	BK	BD	K1	K2	K	QM1	QM2	QM3	QM4
Test case 1											
1	6	6	1.0	1.0	0	1	1	0.5	−0.5	−0.5	0.5
2	3	3	2.5	2.5							
3	5	5	−1.0	−1.0							
4	1	1									
5	2	2									
6	5	5									
7	2	2									
	WW = −0.7071068										
Test case 2											
1	3	3	0.5	0.5	2	2	1	0.5	−0.5	0.5	−0.5
2	3	3	1.5	1.5							
3	3	3	0.5	0.5							
4	3	3									
5	1	1									
6	3	3									
7	1	1									
	WW = 1.2247449										

Table A2. *Cont.*

No.	IK	ID	BK	BD	K1	K2	K	QM1	QM2	QM3	QM4
Test case 3											
1	5	5	0.0	0.0	3	3	4	0.5	−0.5	0.5	−0.5
2	3	3	2.0	2.0							
3	3	3	0.0	0.0							
4	2	2									
5	1	1									
6	4	4									
7	0	0									
	WW = 4.44971919										

Since the parameters IK, ID, BK, and BD are arrays, the first column in Table A2 indicates the array index, while the remaining columns indicate the values of the subroutine input parameters. For example, in the first example, when No. = 3, then IK(3) = 5, ID(3) = 5, BK(3) = −1.0, and BD(3) = −1.0. Elements of these arrays corresponding to quantities such as the quantum numbers n, l, and j of the subshell or all other characteristics describing the subshell that are necessary for the calculation can be found in Section 3.3 of [20]. The other parameters are simple variables; their values in the table are in the row where No. = 1. The value calculated by the subroutine is given in the row WW. For example, in the case of the first example, it is WW = −0.7071068. This subroutine is available from the corresponding author, [G.G.], upon reasonable request.

References

1. Grant, I.; McKenzie, B.; Norrington, P.; Mayers, D.; Pyper, N. An atomic multiconfigurational Dirac-Fock package. *Comput. Phys. Commun.* **1980**, *21*, 207. [CrossRef]
2. Dyall, K.G.; Grant, I.P.; Johnson, C.T.; Parpia, F.A.; Plummer, E.P. GRASP: A general-purpose relativistic atomic structure program. *Comput. Phys. Commun.* **1989**, *55*, 425–456. [CrossRef]
3. Parpia, F.; Froese Fischer, C.; Grant, I. GRASP92: A package for large-scale relativistic atomic structure calculations. *Comput. Phys. Commun.* **1996**, *94*, 249–271. [CrossRef]
4. Jönsson, P.; He, X.; Froese Fischer, C.; Grant, I. The grasp2K relativistic atomic structure package. *Comput. Phys. Commun.* **2007**, *177*, 597–622. [CrossRef]
5. Jönsson, P.; Gaigalas, G.; Bieroń, J.; Froese Fischer, C.; Grant, I. New version: Grasp2K relativistic atomic structure package. *Comput. Phys. Commun.* **2013**, *184*, 2197. [CrossRef]
6. Fischer, C.F.; Gaigalas, G.; Jönsson, P.; Bieroń, J. GRASP2018—A Fortran 95 version of the General Relativistic Atomic Structure Package. *Comput. Phys. Commun.* **2019**, *237*, 184–187. [CrossRef]
7. Fischer, C.F.; Godefroid, M.; Brage, T.; Jönsson, P.; Gaigalas, G. Advanced multiconfiguration methods for complex atoms: I. Energies and wave functions. *J. Phys. B At. Mol. Phys.* **2016**, *49*, 182004. [CrossRef]
8. Jönsson, P.; Godefroid, M.; Gaigalas, G.; Ekman, J.; Grumer, J.; Li, W.; Li, J.; Brage, T.; Grant, I.; Bieroń, J.; et al. An introduction to relativistic theory as implemented in GRASP. *Atoms* **2023**, *11*, 7. [CrossRef]
9. Jönsson, P.; Gaigalas, G.; Fischer, C.F.; Bieroń, J.; Grant, I.; Brage, T.; Ekman, J.; Godefroid, M.; Grumer, J.; Li, J.; et al. GRASP Manual for Users. *Atoms* **2023**, *11*, 68. [CrossRef]
10. Bunge, C.F. Selected configuration interaction with truncation energy error and application to the Ne atom. *J. Chem. Phys.* **2006**, *125*, 014107. [CrossRef]
11. Jitrik, O.; Bunge, C.F. Atomic configuration interaction and studies of He, Li, Be, and Ne ground states. *Phys. Rev. A* **1997**, *56*, 2614–2623. [CrossRef]
12. Gaigalas, G.; Rynkun, P.; Kitovienė, L. Second-order Rayleigh-Schrödinger perturbation theory for the GRASP2018 package: Core-valence correlations. *Lith. J. Phys.* **2024**, *64*, 20–39. [CrossRef]
13. Gaigalas, G.; Rynkun, P.; Kitovienė, L. Second-order Rayleigh-Schrödinger perturbation theory for the GRASP2018 package: Core correlations. *Lith. J. Phys.* **2024**, *64*, 73–81. [CrossRef]
14. Gaigalas, G.; Rynkun, P.; Kitovienė, L. Second-order Rayleigh-Schrödinger perturbation theory for the GRASP2018 package: Core-core correlations. *Lith. J. Phys.* **2024**, *64*, 139–161. [CrossRef]

15. Gaigalas, G.; Rynkun, P.; Kitovienė, L. Second-order Rayleigh-Schrödinger perturbation theory for the GRASP2018 package: Valence-valence correlations. *Lith. J. Phys.* **2025**, *65*, 32–56. [CrossRef]
16. Gaigalas, G.; Rynkun, P.; Kitovienė, L. Second-order Rayleigh-Schrödinger perturbation theory for the GRASP2018 package: Three-particle Feynman diagram contribution to valence-valence correlations. *Lith. J. Phys.* **2025**, *65*, 81–106. [CrossRef]
17. Gaigalas, G.; Rynkun, P.; Kitovienė, L. Second-order Rayleigh-Schrödinger perturbation theory for the GRASP2018 package: Three-particle Feynman diagram contribution to core-valence correlations. *Lith. J. Phys.* 2026, *accepted*. [CrossRef]
18. McKenzie, B.J.; Grant, I.P.; Norrington, P.H. A program to calculate transverse Breit and QED corrections to energy levels in a multiconfiguration Dirac-Fock environment. *Comput. Phys. Commun.* **1980**, *21*, 233–246. [CrossRef]
19. Grant, I.P. *Relativistic Quantum Theory of Atoms and Molecules. Theory and Computation*; Atomic, Optical and Plasma Physics; Springer: New York, NY, USA, 2007. [CrossRef]
20. Gaigalas, G. A program library for computing pure spin-angular coefficients for one- and two-particle operators in relativistic atomic theory. *Atoms* **2022**, *10*, 129. [CrossRef]
21. Gaigalas, G.; Rudzikas, Z.; Froese Fischer, C. An efficient approach for spin-angular integrations in atomic structure calculations. *J. Phys. B At. Mol. Phys.* **1997**, *30*, 3747–3771. [CrossRef]
22. Gaigalas, G. Extension of an efficient approach for spin-angular integrations in atomic structure calculations. *Atoms* **2026**, *14*, 21. [CrossRef]
23. Lindgren, I.; Morrison, J. *Atomic Many-Body Theory*; Springer Series in Chemical Physics; Springer: Berlin/Heidelberg, Germany, 1982; Volume 13.
24. Hubač, I.; Wilson, S. *Brillouin–Wigner Methods for Many-Body Systems*; Springer: Dordrecht, The Netherlands; Berlin/Heidelberg, Germany; London, UK; New York, NY, USA, 2010.
25. Shavitt, I.; Bartlett, R.J. *Many-Body Methods in Chemistry and Physics*; Cambridge University Press: Cambridge, UK, 2009.
26. Uylings, P. *Complex Atoms*; Anton Pannekoek Institute for Astronomy, University of Amsterdam: Amsterdam, The Netherlands, 2021.
27. Gaigalas, G. Irreducible Tensorial Form of the Stationary Perturbation Theory for Atoms and Ions with Open Shells. Ph.D. Thesis, Institute of Physics, Vilnius, Lithuania, 1989. Available online: https://kolekcijos.biblioteka.vu.lt/en/objects/990007058341008452#00001 (accessed on 3 April 2026). (In Russian)
28. Li, Y.T.; Wang, K.; Si, R.; Godefroid, M.; Gaigalas, G.; Chen, C.Y.; Jönsson, P. Reducing the computational load – atomic multiconfiguration calculations based on configuration state function generators. *Comput. Phys. Commun.* **2023**, *283*, 108562. [CrossRef]
29. Si, R.; Li, Y.; Wang, K.; Chen, C.; Gaigalas, G.; Godefroid, M.; Jönsson, P. Graspg—An extension to Grasp2018 based on configuration state function generators. *Comput. Phys. Commun.* **2025**, *312*, 109604. [CrossRef]
30. Froese Fischer, C.; Brage, T.; Jönsson, P. *Computational Atomic Structure—An MCHF Approach*; Institute of Physics Publishing: Bristol, UK, 1997.
31. Gaigalas, G. Diagrammatic Approach to Irreducible Tensorial Operators and its Application to Perturbation Theory. In *Spectroscopy of Autoionized States of Atoms and Ions*; Safronova, U., Ed.; Scientific Council of Spectroscopy: Moscow, Russia, 1985; pp. 43–61. (In Russian)
32. Goldstone, J. Derivation of the Brueckner many-body theory. *Proc. R. Soc. Lond. A Math. Phys. Sci.* **1957**, *239*, 267–279. [CrossRef]
33. Jucys, A.; Bandzaitis, A. *Theory of Angular Momentum in Quantum Mechanics*; Mokslas: Vilnius, Lithuania, 1977.
34. Gaigalas, G.; Kaniauskas, J.; Rudzikas, Z. A Diagrammatic Technique in the Angular Momentum Theory and Second Quantization. *Sov. Phys. Collect.* **1985**, *25*, 3–13.
35. Merkelis, G.; Gaigalas, G.; Rudzikas, Z. Irreducible Tensorial Form and Diagrammatic Representation of the Effective Hamiltonian of an Atom in the First Two Orders of the Stationary Perturbation Theory. *Sov. Phys. Collect.* **1985**, *25*, 14–31.
36. Judd, B. *Second Quantization and Atomic Spectroscopy*; The Johns Hopkins Press: Baltimore, MD, USA, 1967.
37. Rudzikas, Z.; Kaniauskas, J. *Quasispin and Isospin in the Theory of the Atom*; Mokslas: Vilnius, Lithuania, 1984.
38. Rudzikas, Z. *Theoretical Atomic Spectroscopy*; Cambridge Monographs on Atomic, Molecular and Chemical Physics; Cambridge University Press: Cambridge, UK, 1997. [CrossRef]
39. Gaigalas, G.; Rudzikas, Z.; Froese Fischer, C. Reduced coefficients (subcoefficients) of fractional parentage for p-, d-, and f-shells. *At. Data Nucl. Data Tables* **1998**, *70*, 1–39. [CrossRef]
40. Gaigalas, G.; Fritzsche, S.; Rudzikas, Z. Reduced Coefficients of Fractional Parentage and Matrix Elements of the Tensor W(kqkj) in jj-Coupling. *At. Data Nucl. Data Tables* **2000**, *76*, 235–269. [CrossRef]
41. Gaigalas, G.; Rudzikas, Z. On the secondly quantized theory of the many-electron atom. *J. Phys. B At. Mol. Phys.* **1996**, *29*, 3303–3318. [CrossRef]
42. Kaniauskas, J.M.; Rudzikas, Z.B. Quasi-spin method for jj coupling in the theory of many-electron atoms. *J. Phys. B At. Mol. Phys.* **1980**, *13*, 3521. [CrossRef]

43. Kramida, A.; Ralchenko, Y.; Reader, J.; NIST ASD Team. *NIST Atomic Spectra Database*, Version 5.12; National Institute of Standards and Technology: Gaithersburg, MD, USA, 2024. Available online: https://www.nist.gov/pml/atomic-spectra-database (accessed on 10 February 2026).
44. Kitovienė, L.; Gaigalas, G.; Rynkun, P.; Tanaka, M.; Kato, D. Theoretical investigation of the Ge isoelectronic sequence. *J. Phys. Chem. Ref.* **2024**, *53*, 033101. [CrossRef]
45. Rynkun, P.; Banerjee, S.; Gaigalas, G.; Tanaka, M.; Radžiūtė, L.; Kato, D. Theoretical investigation of energy levels and transition for Ce IV. *Astron. Astrophys.* **2022**, *658*, A82. [CrossRef]
46. Gaigalas, G.; Rynkun, P.; Banerjee, S.; Tanaka, M.; Kato, D.; Radžiūtė, L. Theoretical investigation of energy levels and transitions for Pr IV. *Mon. Not. R. Astron. Soc.* **2022**, *517*, 281–293. [CrossRef]
47. Suzuki, N.; Kosugi, S.; Ito, Y.; Inoue, N.; Nagoshi, T.; Kuze, N.; Harries, J.R.; Sullivan, J.P.; Nagata, T.; Sokell, E.; et al. Probing electron correlation through radiative lifetime measurements upon inner-valence photoionization of Ne and Ar. *J. Phys. B At. Mol. Opt. Phys.* **2016**, *49*, 145002. [CrossRef]
48. Lauer, S.; Liebel, H.; Vollweiler, F.; Schmoranzer, H.; Lagutin, B.M.; Demekhin, P.V.; Petrov, I.D.; Sukhorukov, V.L. Lifetimes of the $ns^1\ np^6\ ^2S_{1/2}$ states of singly ionized argon, krypton and xenon. *J. Phys. B At. Mol. Opt. Phys.* **1999**, *32*, 2015. [CrossRef]
49. Froese Fischer, C.; Tachiev, G.; Irimia, A. Relativistic energy levels, lifetimes, and transition probabilities for the sodium-like to argon-like sequences. *At. Data Nucl. Data Tables* **2006**, *92*, 607–812. [CrossRef]